

**MONITORING BLOOD FLOW IN ANIMAL MODELS USING A CAMERA-
BASED TECHNIQUE**

A Dissertation submitted in partial fulfillment
of the requirements for the degree of
Doctor of Philosophy

by

DHARMINDER SINGH LANGRI

B. Tech. Instrumentation Engineering, Shree Ramanand Teerth Marathwada University, 2015
M.S. Biomedical Engineering, Wright State University, 2019

2023

Wright State University

WRIGHT STATE UNIVERSITY
COLLEGE OF GRADUATE PROGRAMS AND HONORS STUDIES

21st April 2023

I HEREBY RECOMMEND THAT THE DISSERTATION PREPARED UNDER MY SUPERVISION BY Dharminder Singh Langri ENTITLED Monitoring Blood Flow in Animal Models using a Camera-Based Technique BE ACCEPTED IN PARTIAL FULFILLMENT OF THE REQUIREMENTS FOR THE DEGREE OF Doctor of Philosophy.

Ulas Sunar, PhD.
Dissertation Director.

Ahsan Mian, Ph.D.
Program Director, Ph.D. in Engineering.

Shu Schiller, Ph.D.
Interim Dean, College of
Graduate Programs & Honors Studies

Committee on Final Examination:

Ulas Sunar, Ph.D.

Keiichiro Susuki, Ph.D.

Tarun Goswami, Ph.D.

Robert Lober, MD, Ph.D.

ABSTRACT

Langri, Dharminder Singh. Ph.D., Engineering, Ph.D. Program, Wright State University, 2023. Monitoring Blood Flow in Animal Models using a Camera-Based Technique.

Blood flow plays a critical role in maintaining tissue health, as it delivers nutrients and oxygen while removing waste products. Regulation of blood flow is essential to ensure that tissues receive adequate oxygen and nutrients. Therefore, the measurement and regulation of blood flow have many applications in both research and clinical settings.

Optical techniques have become increasingly popular for measuring blood flow due to their non-invasive, continuous, and relatively inexpensive nature. These techniques use light to measure blood flow and have several advantages over traditional methods, such as ultrasound and magnetic resonance imaging (MRI). Optical techniques can provide more detailed information about blood flow, including its speed and direction, which can help diagnose and monitor diseases, as well as assess the effectiveness of treatments.

During my Ph.D., I focused on developing a new optical technique for measuring blood flow using laser speckle contrast imaging and a fiber-camera-based approach. This technique is particularly well-suited for measuring blood flow in deep tissues, such as the brain, which is challenging to access using traditional methods. The device I developed is flexible and can be modified for various purposes, such as monitoring cerebral blood flow at the bedside.

One of the challenges of current optical blood flow measurement devices is their

cost for high-density configurations, which is due to the cost of individual detectors. To address this issue, I proposed a new multi-channel, low-cost, high-density imaging system based on a scientific CMOS detector. This system uses fiber-coupling to allow individual pixels to act as detectors, enabling cost-effective high-density imaging.

My thesis included several chapters that provided motivation, theory, instrumentation, and validation for this system. In Chapter 1, I provided the motivation for developing a fiber-based laser speckle contrast imaging technique. Chapter 2 covered the theory behind the diffuse optics, laser speckle contrast imaging (LSCI) method, and Diffuse Correlation Spectroscopy (DCS). Chapter 3 focused on the instrumentation part of the system, including the design and construction of the fiber-camera based approach. Chapter 4 consisted of the validation part of the system, in which I tested the system using a series of dynamic flow phantom experiments, as well as mice and human cerebral blood flow measurements.

The validation experiments demonstrated that the system can measure blood flow in deep tissues with high contrast and resolution, which could provide new insights into diseases and treatments. This wearable, high-density optical neuroimaging technology is expected to have many applications in various areas, such as pediatric neuroimaging and human performance assessment in military research. Additionally, this system could pave the way for the development of new diagnostic and monitoring tools that are cost-effective, non-invasive, and capable of providing high-resolution imaging of blood flow in deep tissues.

Contents

1	Introduction	1
1.1	Traumatic Brain Injury	1
1.2	Muscular Dystrophy	3
1.3	Current Imaging Approaches	5
1.4	Proposed Solutions with respect to imaging techniques	7
1.5	Objective of the Thesis	8
1.6	Thesis Outline.....	9
2	Diffuse Optical Theory.....	10
2.1	Light propagation in tissues	10
2.2	Tissue Optical Properties	12
2.2.1	Light absorption	12
2.2.2	Light scattering.....	14
2.3	Wavelength selection.....	16
2.4	Laser Speckle Contrast Imaging	18
2.4.1	Speckle	18
2.4.2	The Model	19
2.5	Diffuse Correlation Spectroscopy.....	23
3	Instrumentation	26
4	Device validation and results.....	34
4.1	Testing for laser stability	34
4.2	Signal to noise ratio (SNR) testing	35
4.3	Dynamic flow phantom linearity testing.....	38
4.4	Human infant head mimicking phantom	40
4.5	Muscle blood flow occlusion experiment.....	42
4.6	Muscular Dystrophy disease Mouse Model	43

4.7	Traumatic Brain Injury mouse model experiment	46
4.8	Towards Human Brain Measurement	52
5	Conclusions & Future works	54
5.1	Conclusions.....	54
5.2	Future works	55
	Bibliography.....	57

List of Figures

2.1	Different Photon paths taken when light incident on tissue surface	11
2.2	Incident photons of light being absorbed and attenuated due to medium's absorption	13
2.3	Incident photons of light being scattered due to medium's scattering.....	14
2.4	Absorption coefficient spectrum of different chromophores on human body....	17
2.5	Laser speckle pattern and the physics behind it.....	19
2.6	Image of rodent brain before and after laser speckle analysis of the acquired image.....	20
3.1	Block diagram of the setup.....	27
4.1	Laser power stability results... ..	35
4.2	SNR plots	
4.2.1	As a function of source detector separation of the system	36
4.2.2	As a function of signal counts for the camera... ..	38
4.3	Flow Phantom experiment setup and results... ..	40
4.4	Human infant head mimicking experiment setup and results.....	41
4.5	Human arm cuff occlusion experiment setup and results... ..	43
4.6	Mouse muscle tetanic contraction experiment setup	44
4.7	Mouse muscle tetanic contraction experiment blood flow results.....	45
4.8	Traumatic brain injury model setup in mice model	48
4.9	Relative blood flow results in control and TBI induced mice model... ..	49
4.10	Comparison of blood flow change in control and TBI induced group of mice	50
4.11	Head of bed experiment on adult human, it's setup and results... ..	53

List of Tables

1.1	Comparison between the Laser Doppler, Transcranial Doppler and Laser Speckle	6
-----	--	---

Abbreviation's List

μ_a	Absorption Coefficient
μ_s'	Scattering Coefficient
<i>ADC</i>	Analog to Digital Conversion
<i>ANOVA</i>	Analysis of Variance
<i>ANSI</i>	American National Standard Institute
<i>APD</i>	Avalanche photodiode
<i>CBF</i>	Cerebral Blood Flow
<i>CT</i>	Computed Tomography
<i>CW - DCS</i>	Continuous Wave Diffuse correlation spectroscopy
<i>D/BMD</i>	Duchenne and Becker Muscular Dystrophy
<i>DAQ</i>	Data Acquisition Card
<i>DCS</i>	Diffuse Correlation Spectroscopy
<i>DLPF</i>	Dorsolateral Prefrontal Cortex
<i>DPSS</i>	Diode-Pumped Solid State
<i>GUI</i>	Graphical User Interface
<i>HbO₂</i>	Oxy-hemoglobin
<i>HHb</i>	Deoxy-hemoglobin
<i>ICP</i>	Intracranial Pressure
<i>ICU</i>	Intensive Care Units
<i>IEEE</i>	Institute of Electrical and Electronics Engineers
<i>LDF</i>	Laser Doppler Flowmetry
<i>LSCI</i>	Laser Speckle Contrast Imaging
<i>MD</i>	Muscle Dystrophy
<i>MRI</i>	Magnetic Resonance Imaging
<i>ND</i>	Neutral Density
<i>NICU</i>	Neurological Intensive Care Units
<i>NIR</i>	Near-Infrared
<i>NIRS</i>	Near-Infrared Spectroscopy
<i>nNOS</i>	neuronal Nitric Oxide Synthase
<i>OD</i>	Optical Density
<i>PET</i>	Positron Emission Tomography
<i>PMT</i>	Photomultiplier Tube
<i>rCBF</i>	relative Cerebral Blood Flow
<i>sCMOS</i>	Scientific Complementary Metal - Oxide - Semiconductor
<i>SD</i>	Source - Detector
<i>SDS</i>	Source Detector Separation

<i>SWIR</i>	Short-Wave Infrared
<i>TBI</i>	Traumatic Brain Injury
<i>TCD</i>	Transcranial Doppler Ultrasound
<i>US</i>	Ultrasound

Acknowledgment

I would like to take this opportunity to express my deepest appreciation to my thesis advisor, Dr. Ulas Sunar, for his exceptional support, guidance, and patience throughout the duration of my thesis project. From the very beginning, he provided me with invaluable insights into the research process and encouraged me to pursue my interests and passions. He was always available to discuss my ideas, offer constructive feedback, and help me navigate any challenges that arose along the way. His dedication to my academic growth and success has been truly remarkable, and I feel fortunate to have had such an inspiring mentor.

In addition to my thesis advisor, I would also like to acknowledge the committee members, Dr. Keiichiro Susuki, Dr. Tarun Goswami and Dr. Robert Lober for agreeing to be a part of my thesis committee and offering valuable suggestions. I would like to thank Dr. Emily Dudley, Mr. Dale Goss and all the staff members of the Department of Laboratory Animal Resources for their valuable help and support for all the animal model experiments performed and used to help achieve my thesis. I would like to acknowledge the faculty and staff members of the Biomedical Engineering department for their invaluable contributions to my education. Throughout my studies, they challenged me to think critically, pushed me to expand my intellectual horizons, and provided me with the tools and knowledge necessary to succeed in my research. Their commitment to academic excellence has been a constant source of motivation and inspiration, and I am grateful for the opportunity to learn from such distinguished scholars and educators.

I would also like to extend my gratitude to my colleagues and friends for their unwavering support, encouragement, and companionship throughout this journey. They have been my sounding board and my confidants, offering advice, sharing their own experiences, and cheering me on through the highs and lows of the research process. I feel blessed to have had such a supportive and inspiring community, and I will always treasure the memories we have created together.

Last but not least, I am immensely grateful to my family, my mom and dad, Mrs. Jay Kaur Langri and Mr. Tejinder Singh Langri, my brother, Mr. Harminder Singh Langri, and Ms. Mallory Hollister for their unconditional love, understanding, and unwavering support. They have been my rock throughout this journey, providing me with emotional and financial support, cheering me on from the sidelines, and reminding me of the bigger picture when I felt overwhelmed or discouraged. Their sacrifices and encouragement have been the driving force behind my success, and I could not have achieved this without their love and support.

In conclusion, I express my heartfelt appreciation to everyone who has played a role in my success. Without their guidance, support, and encouragement, I would not have been able to complete this project and achieve my academic goals.

Dedicated to

My Mother, Jay Kaur Tejinder Singh Langri. Thank you for always loving and supporting me whenever I needed you.

Chapter 1 - Introduction

Secondary brain injuries are usually caused by cerebral ischemia in patients with neurological conditions such as traumatic brain injuries (TBI) and strokes. Thus, to avoid temporary or permanent brain damage due to abnormal cerebral blood flow (CBF) due to such conditions, it is essential to monitor the neurological conditions of a patient in Neurological Intensive Care Units (NICU) or Intensive Care Units (ICU), where fluctuations in CBF can be detected and timely interventions can be taken to regulate CBF in the patient, thus reducing the chances of developing any secondary brain injury or damage. Due to these reasons, it is very important that there is a method to monitor the blood flow at the bedside in NICUs or ICUs.

1.1 Traumatic Brain Injury

There is a critical need to accurately predict the risk of neurodevelopmental impairments, including motor, cognitive, and language impairments, in very preterm infants early after birth. Real-time evaluation of neurophysiology at the bedside will provide invaluable information that can allow for earlier detection of brain injuries and uncover their underlying mechanisms, such as hypoxia/ischemia. This information will lead to a possible prevention of brain injuries and interventions that target the underlying mechanism rather than mitigating the functional outcomes of

established injuries. Diffuse optical imaging can be used as an intraoperative intervention technique to recognize these anomalies in the beginning stage; therefore, hemodynamic monitoring is critical, especially in the transition period to extrauterine life and during the accompanying after days.

Patients with TBI are susceptible to cerebral ischemia leading to secondary brain injury. Timely interventions to restore adequate CBF can avoid brain damage in the neurological intensive care unit (NICU), if CBF reductions can be detected. Therefore, continuous CBF measurement at the bedside is crucial.

Up to 30% of deadly injuries and long-term disabilities in the United States are caused by TBI, which affects more than 3 million US citizens and brings the annual cost up to 80 billion [1]. Deaths, hospitalizations, and emergency visits to hospitals related to TBI increased by a factor of 53% from 2006 to 2014. An average of 155 deaths each day due to TBI in the United States alone was recorded in 2014. Due to the lack of adequate means of diagnosis and timely reporting, approximately 5.3 million people in the United States alone are forced to live with long-term disabilities due to TBI. These effects can last for a few days to the rest of their life. TBI can lead a patient to cognitive impairment, loss of basic senses such as vision, hearing, or smell, loss of movement or emotional functioning (e.g., personality changes, depression). These issues cost more than ~\$80 billion approximately for treatment and rehabilitation.

Damage due to TBI can be caused due to several events or reasons, such as traffic accidents, sports injuries, mechanical falls due to daily activities, military service injuries, criminal incidences, and many others. To design effective and appropriate

treatment plans, it is crucial to evaluate the severity and complications associated with such a brain injury. Complications associated with such injuries are composed of and are not limited to changes in levels and loss of memory, consciousness, difficulty maintaining balance and orientation, confusion, fluctuations and loss of visual, olfactory, auditory and tactile senses, mental and emotional fluctuations, and eventually death. Most current diagnoses of injuries related to TBI and its severity are indicated by methods such as speech tests, language tests, neurophysiological tests, cognitive assessments, functional assessments with the help of the Glasgow Coma Scale and self-reporting symptoms and scales. These are not clear indicators of the localization and severity of injury due to TBI [71].

1.2 Muscular Dystrophy

Muscular Dystrophy is caused by mutated genes, resulting in decreased mobility and muscle weakness and degeneration, causing difficulty in daily routine. Around 2,50,000 people in the United States have been estimated to be affected by muscular dystrophy [39, 40]. Duchenne and Becker Muscular dystrophy (D/BMD) are the most common among muscular dystrophies. They are debilitating genetic disorders that predominantly affect men. The prevalence of D/BMD is estimated to be around 1 in 5000 boys [42, 43]. These disorders are caused by mutations in the dystrophin gene on the X chromosome, leading to a progressive loss of muscle strength and function. Although both D / BMD are the result of mutations in the same gene, Becker muscular dystrophy is generally less severe than Duchenne muscular dystrophy due to a specific mutation that preserves a partially functional dystrophin protein [42, 44, 45].

Dystrophin is an essential protein that plays a crucial role in stabilizing the cell membrane of muscle cells. In D/BMD, the absence or dysfunction of dystrophin results in the failure of the dystroglycan complex, leading to the disruption of the neuronal nitric oxide synthase (nNOS) signaling pathway. This pathway is responsible for mediating the dilation of blood vessels following exercise to ensure adequate blood flow to the exercised muscle. In D/BMD, the impairment of this pathway leads to exercise-induced muscle ischemia [42, 46].

Restoring the nNOS pathway and repairing functional muscle ischemia is a potential therapeutic target in the treatment of D/BMD. Animal and human clinical trials have shown that therapeutic correction of the impaired nNOS pathway can restore muscle blood flow. This has led to ongoing efforts to develop new treatments and therapies that target this pathway.

Blood flow to muscles is typically measured indirectly in human trials, either through color Doppler evaluation of the brachial artery or through evaluation of muscle oxygenation using infrared spectroscopy. Direct measurement of intramuscular blood flow using ultrasound is possible, but requires intravenous contrast agents and a rigorously controlled research protocol that limits its application at the bedside or in the clinic.

Overall, the identification of the nNOS pathway as a potential therapeutic target in D/BMD has opened up new avenues for the development of treatments and therapies that could potentially improve the lives of individuals living with these debilitating disorders. Thus, muscular blood flow could be used to assess the efficiency of the therapy provided to improve intramuscular blood flow to intervene

and counteract the progression of this condition [41, 42].

1.3 Current Imaging Approaches

Various imaging technologies, such as magnetic resonance imaging (MRI), computed tomography (CT), and positron emission tomography (PET), and ultrasound (US) are available for clinical use including for TBI and MD. These imaging techniques are very expensive and bulky, although they are non-invasive, they are not suitable for continuous bed side monitoring due to slow scanning speeds [2]. There are alternate methods of evaluating cerebral blood flow by measuring the intracranial pressure (ICP), for this method it is required that a flow meter or pressure transducer probe is inserted in the skull into the cortex by drilling a hole in the skull of the patient, which can risk infection, bleeding and haemorrhage [1, 3, 4].

Other such modalities which are used for measuring blood flow are Laser Doppler Flowmetry (LDF) and Transcranial Doppler Ultrasound (TCD). Laser Doppler and Ultrasound Doppler fundamentally follow a similar principle known as the Doppler effect to quantify the flow velocity. The Doppler effect is the change of frequency that occurs when there is relative movement between the source and the detector of a wave. The detected wave (the light wave (for the Laser Doppler case) or sound wave (for the Ultrasound Doppler case)) has frequency shifted based on the speed of the blood cell. Higher speed leads to a larger Doppler frequency shift. The most recognizable regular model is the drop in pitch (based on frequency) as a sound source moves past by. An especially genuine model is an ambulance or fire engine with its siren sounding [5, 6].

Table 1.1 Comparison between the Laser Doppler, Transcranial Doppler and Laser Speckle

Ultrasound Doppler	Laser Doppler	Laser Speckle
Contact with coupling agent required	Probe Stability required and contact is needed.	No contact required
Non-detection zone induced by frequency of ultrasound	Limited Detection Zone	Full Field detection possible
Low Spatial & Temporal resolution	Low Spatial & Temporal resolution	Higher Spatial and Temporal Resolution
Local Area Monitoring	Single Point Monitoring	Large View Field
Relatively fast	Slow	Fast

There are some optical methods available in the market commercially named Near-Infrared Spectroscopy (NIRS), which operates on the diffuse optical technique, which allows bedside, non-invasive continuous monitoring of hemodynamic in vivo. This technique measures the changes in concentration of different chromophores, but fails to measure the absolute number and cannot directly calculate the continuous CBF.

Laser Doppler scanning and speckle contrast imaging have shown importance for blood flow studies in animals, but require that the skull be cleared out or reduced extensively. Although effective, its regular use is limited due to availability, size and cost of the instruments, and the difficulty of making assessments for bedside monitoring, and in the intensive care unit (ICU) or operating rooms.

1.4 Proposed Solution with respect to Imaging Techniques

In this thesis, an optical blood flow for relatively deep tissue is investigated. The current standard optical technology for measuring in-vivo blood flow and dynamic motion is continuous wave diffuse correlation spectroscopy (DCS). Although DCS can be used for CBF measurement, an Avalanche photodiode (APD) or photomultiplier tube (PMT) needs to be used as detectors to measure at one single point. For potential imaging applications, which will require many detectors, the DCS approach is limited due to significantly costly detectors. Furthermore, DCS is usually signal limited, and the acquisition is slow (~1-5 seconds). It will be even significantly slower if one wants to develop a DCS multi-source multidetector imaging DCS-system (~ >10 seconds/image). This limitation of DCS system limits scanning of multiple channels, and integration time using this approach detectors. To overcome this limitation, here I propose a sCMOS-based fiber-camera setup that can incorporate multiple detectors (~ 25) in one single camera, making it highly cost-effective compared to DCS. Also, this will increase both temporal and spatial resolution since there is an increase in detectors, and the exposure time required can be reduced to 5 to 20 milliseconds, which is a significant advantage over DCS. Acquisition of multichannel data also opens the opportunity to perform a topographic image in the target region, which will be very helpful to determine local blood flow using high-density imaging.

1.5 Objective of the Thesis

The first objective of this thesis is to develop a prototype of high-density camera-based blood flow imaging system, that can calculate the CBF non-invasively and have capability of supporting bed side continuous blood flow monitoring. For this purpose, to assist working of this device, custom probes will be designed, developed and printed using CAD and 3-D printers. Designing the custom probes will help with specific tailored applications. The system will be characterized, validated, and optimized firstly using the tissue simulation static and dynamic phantoms to determine the signal-to-noise ratio, stability and accuracy of the system. Diffuse Correlation Spectroscopy (DCS) system will be used as an established optical blood flow system for a comparison.

The second objective of this study is to characterize and optimize the developed system using phantoms and computer simulations. For this purpose, several dynamic flow phantoms and in-vivo blood pressure cuff occlusion experiments were performed and the data was captured using the developed system, analyzed and compared with the lab standard DCS system, to validate the performance of the Fiber-Camera LSCI system in flow measurement of deep tissue.

The third objective of this thesis is to collect data from healthy and TBI population in mice and to study the case to see if there is a significant difference in blood flow parameters in both cases. After the characterization of the system was done, various tests were performed using this system to validate the working and reliability of the system. Various phantom and in-vivo tests were done and compared with lab-standard DCS device to validate the working of the system.

1.6 Thesis Outline

The first chapter of this thesis, as mentioned above, demonstrated the technical and clinical significance of developing an LSCI device using sCMOS.

The theory, background, and principle behind laser speckle imaging, and the physical and optical properties affecting them, will be discussed in the second chapter.

The third chapter of this thesis contains the description to all the elements related to building the Camera-based LSCI system, instrumentation, assembly and interface along with demonstrations with help of block diagrams.

The fourth chapter consists of techniques and studies used for device validation along with their results and comparison with the corresponding laboratory standard devices for various phantom, animal studies conducted.

Finally, brief discussion, conclusion and future directions of this thesis and the developed device along with its results construct the fifth chapter of this thesis.

Chapter 2 – Diffuse Optical Model

In this chapter, we will discuss the equations, theory and principles behind diffuse optical imaging, and how light interacts in a medium, and based on this information how blood flow can be calculated in human or animal models. This chapter will discuss how light interacts and propagates in tissue, the significance of optical properties of a given medium, and how it is helpful in calculating the flow of that medium or system. Further, two methods to quantify blood flow in deep tissues, namely Continuous Wave Diffuse Correlation Spectroscopy (CW - DCS) and Laser Speckle Contrast Imaging (LSCI), are discussed briefly.

2.1 Light Propagation in tissues

For the wavelength of light belonging to the NIR region (600 – 1000 nm), biological tissues are relatively transparent as compared to other wavelengths [8,14]. Thus, the importance and significance of optical methods in applications such as noninvasive diagnosis of studies related to human or animal tissues, especially the brain, have been established for over decades. This wavelength window is optimized range so that the chromophores in human tissues such as oxygenated and deoxygenated hemoglobin, lipids and water absorbs less light and hence giving the option of optical analysis and imaging for a larger depth as compared to other wavelength windows, which is helpful in examining various tissues, especially cortical region [8].

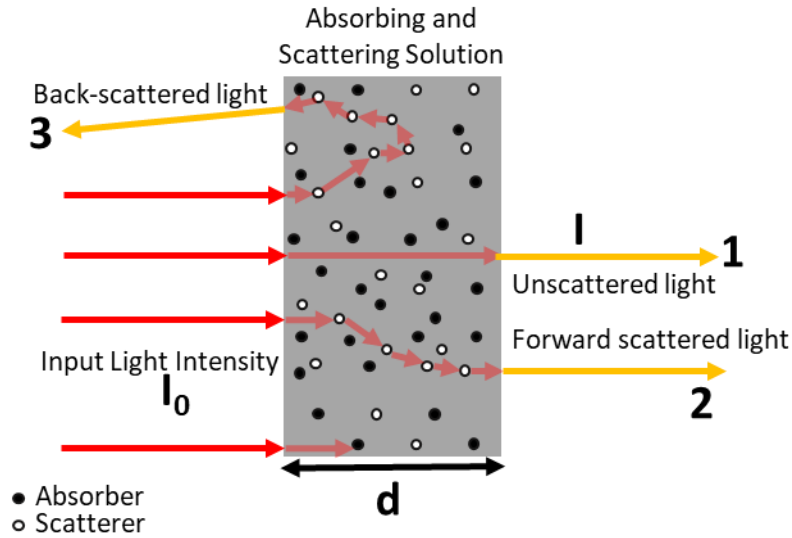


Figure 2.1. Different photon path taken when incident on tissue surface. 1) Un-scattered photon/light travelling straight without getting absorbed or scattered, 2) The photon exiting the sample in transmission mode after undergoing multiple scattering event and getting Forward scattered, 3) The photon exiting the sample in reflectance mode after undergoing multiple scattering event and getting Back-scattered.

Photons that are incident on the surface of tissue follows certain characteristics based on the scattering and absorbing components present in the sample or tissue because of the chromophores present in the tissue. The incident light intensity or the photons can be divided into three categories namely absorbed, transmitted, and reflected light intensity, and the incident light intensity is the addition of all the three intensities listed above. As described in the figure 2.1. above, the light intensity which is incident on the sample can be transmitted either straight without being absorbed, absorbed due to absorbing components present, and can undergo multiple scattering events to result in either forward scattered light or back-scattered light intensity. For non-invasive optical imaging and studies, usually the back-scattered light is studied for in-vivo studies where the reflectance geometry for source and detectors is used to transmit the light into the tissue and then collect the back scattered light through the

detectors to determine the parameters such as the amount of concentration of chromophores in the tissue or the relative flow in it. All the parameters listed above are wavelength dependent [13].

In the optical properties of following sections, the scattering and absorption and its effect on the propagation of light within the medium or a given sample will be discussed in detail along with some equations related to them, and how they can be used to determine the optical properties of a tissue based on the intensity of light that is received at the receiving end.

2.2 Tissue Optical Properties

2.2.1 Light absorption

As first observed and described by Bourger in 1729 followed by Lambert in 1760 that the relation of light absorption in an absorbing and non-scattering medium based on medium's thickness can be quantified. According to them, a small fraction dI of light that has the intensity I passed is absorbed if I passes through the medium consisting of successive layers with thickness δd , [7,8]. This is demonstrated in Figure 2.2.

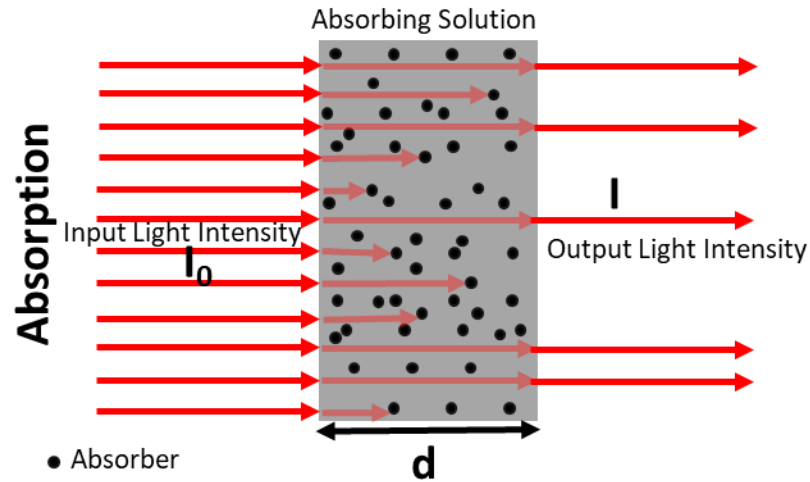


Figure 2.2. Incident light intensity (I_0) being absorbed and attenuated to light intensity (I), after passing through an absorbing medium having thickness d and absorption coefficient (μ_a).

According to the expression given by Lambert-Bouguer.

$$\frac{dI}{I} = -\mu_a * \delta d \quad (2.1)$$

After Integrating, we get

$$I = I_0 e^{(-\mu_a * d)} \quad (2.2)$$

Where, $-\mu_a$ is the absorption coefficient (cm^{-1}) of the medium through which incident light is passed. The absorption coefficient can also be described as the probability of the photon getting absorbed after travelling a unit length in the specified medium. Absorption path length, which is inverse of absorption coefficient (μ_a) given as $1/\mu_a$ having units in cm, is the ability of photon to travel in the same specified

medium without being absorbed.

2.2.2 Light scattering

Similar to total internal reflection due to change in refractive index of materials, mismatching of the refractive index on cellular level causes light scattering in most of the tissues, internal cell organelles and the cell membranes causing major scattering [7,9]. Scattering is an important phenomenon which helps with diffusion of the light, proving deep and thicker tissues. Even in tissues as thin as a fraction of millimeter, there is a high probability of incident photons scattering multiple times before reaching the boundary of the sample [8].

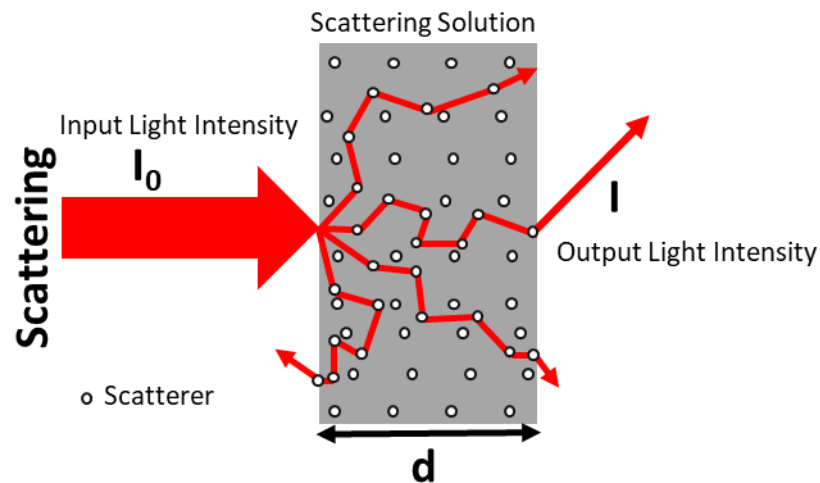


Figure 2.3: Ray diagram of the photon path after multiple scattering events due to the scattering component present in the medium. After scattering, the incident photons increase their pathlength and are detected by the detector with decreased intensity (I), which was initially the incident intensity (I_0).

Scattering causes photons to deviate from their original path, causing the photons to increase their path length and also alter their path from original direction of

propagation, and therefore causing the chances of photons being absorbed in the tissue to increase due to multiple scattering in the given medium, as described in Figure 2.3. Due to this effect of multiple scattering, out of all the photons from incident light, some photons might reflect back, some may pass through unaffected, and some may change their direction.

The factors that affect scattering in brain are wavelength of the incident light, oxygen (or any other chromophore) concentration in the tissue and gestational age [9]. The protein content and lipid content, which increases up to 7 times more in white matter of brain, in adults since childhood, which are significantly high contributes significantly to the increased scattering in the white matter of brain [11].

Let's assume that the medium has only a scattering component in it that has a scattering coefficient μ_s , then the intensity of transmitted light I , after passing through thickness d of the medium, initially having incident intensity I_o can be described as follows.

$$I = I_o e^{(-\mu_s * d)} \quad (2.3)$$

Scattering path length, which is inverse of scattering coefficient μ_s given as $1/\mu_s$ having units in cm, is the ability of photon to travel in the same specified medium without being scattered again [8]. In simple terms, the overall path of photon can be approximated by the linear combination of absorption and scattering coefficient and the transport coefficient (μ_t) can be illustrated for single scattering event as follows [10].

$$\mu_t = \mu_a + \mu_s \quad (2.4)$$

But in biological tissues or even in any medium, photons scatter multiple times, and hence the expression above for single scattering cannot be used in practical expressions.

The reduced scattering coefficient, μ'_s , which is inverse of the distance travelled by a single photon before completely randomizing, or can also be called one random walk, characterizes the scattering in practical applications [8,10]. Reduced scattering coefficient can be expressed as product of scattering coefficient with factor $(1-g)$, where anisotropy factor, g , is the mean of scattering angles and is representation of phase function and expressed as follows [8].

$$\mu'_s = \mu_s(1 - g) \quad (2.5)$$

Hence based on the calculated reduces scattering coefficients above, the reduced transport coefficient can also be expressed as:

$$\mu'_t = \mu'_s + \mu_a \quad (2.6)$$

2.3 Wavelength Selection

Wavelengths of light in the NIR region have been observed to penetrate deeper within the biological tissues giving penetration depth of about 2 cm in reflectance geometry, which is relatively higher than most other bands of wavelengths of light. As evident from the absorption spectrum given in Figure 2.4. below, the absorption coefficient of chromophores such as water, oxygenated and deoxygenated hemoglobin, lipids, bile and melanin present in tissues, above the wavelength of 900 nm are high

causing more light to be absorbed within the tissue causing the reduction in penetration depth of the incident light and hence limiting the scanning depth using diffuse optical methods. Similarly light wavelengths below 700 nm are susceptible to higher scattering and causing similar issue of penetration depth [13]. The reason stated above is why the wavelengths belonging to NIR region, are chosen for optical imaging since deeper penetration is possible within this window of wavelength, making it an optimal choice for diffuse optical studies.

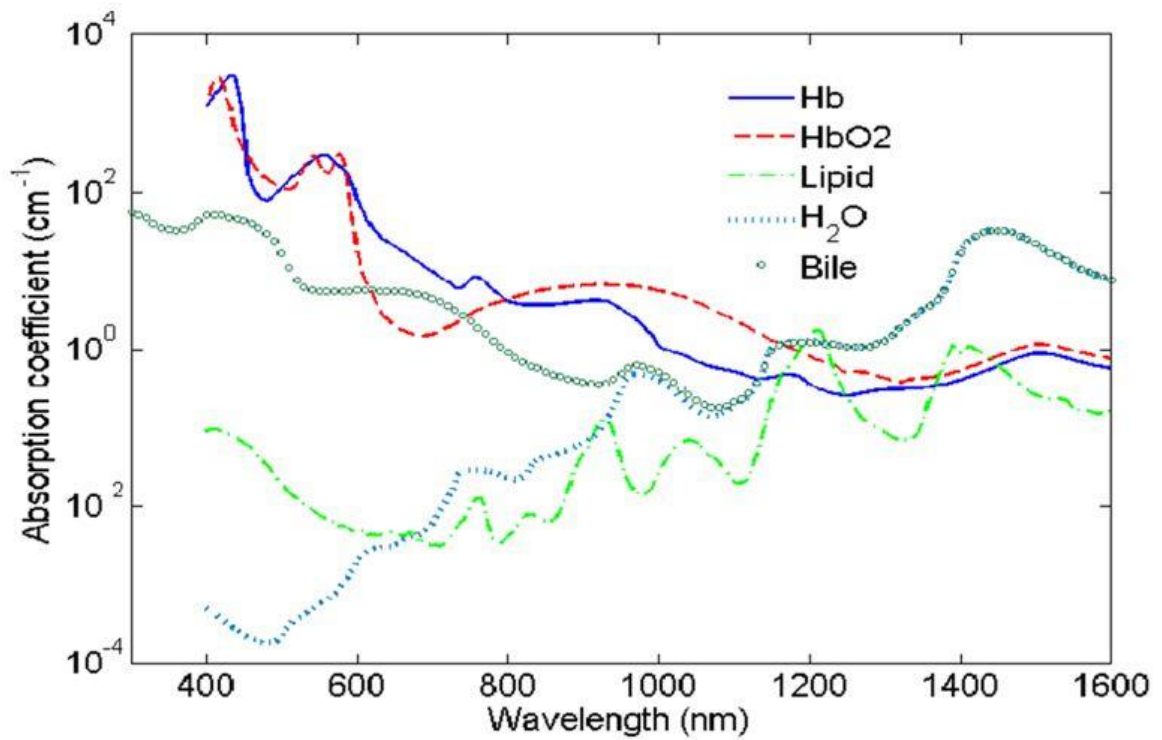


Figure 2.4 The absorption coefficient spectrum of different chromophores present in the human body.

2.4 Laser Speckle Contrast Imaging

2.4.1 Speckle Phenomena

After the invention of laser, it was observed that when the laser is illuminated on objects with a little rough surface, there was formation of a pattern of dark and bright spots in the form of tiny granular pattern, which started attracting attentions of researchers working in the field at that time [18, 19, 20, 21]. Since the pattern resembled a granular pattern, this was called granularity, which was later termed as speckle, and was widely used. The relationship between the coherent nature of laser being used and the surface being illuminated with the speckle pattern was being studied by various researchers [22]. The researchers tried to remove the speckle pattern from the acquired images since it was thought to be affecting and reducing the resolution of the images acquired [23, 24, 25, 26]. Later it was found that there are several uses for the analysis of this granular speckle pattern and one of them is to measure blood flow [27].

As it can be seen in figure 2.5.(a) when a coherent laser is illuminated on slightly rough surface, the light is scattered to form inhomogeneous random dark and bright spots called speckle pattern. The same phenomenon is observed when the light is collected after being diffused through a medium or any biological tissues. This phenomenon can be further explained by young's double slit experiment which also explains the wave nature of light. When the laser is illuminated each wave will travel

different distances if they are propagated in a diffuse medium, due to multiple scattering events occurring because of the scattering due to randomly distributed particles present in the medium through which light is being propagated. When they finally meet on the surface, they will create interference patterns because of the wave nature of the light. When two light waves cause a constructive interference, a bright spot is formed and when two light waves cause a destructive interference, a dark spot, as can be seen in Figure 2.5.(b), this pattern is called the speckle pattern [16].

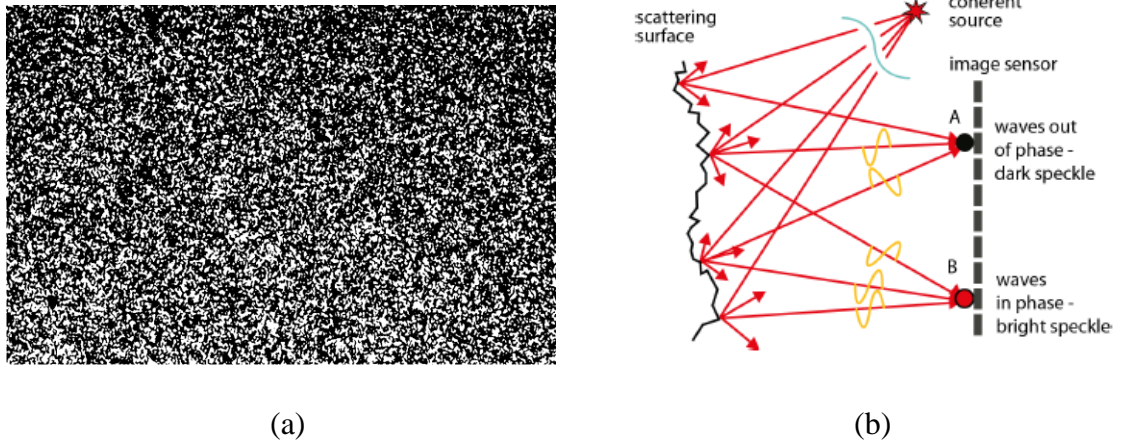


Figure 2.5: Laser speckle. (a) Typical laser speckle pattern, (b) Physics behind laser speckle formation.

2.4.2 The Model

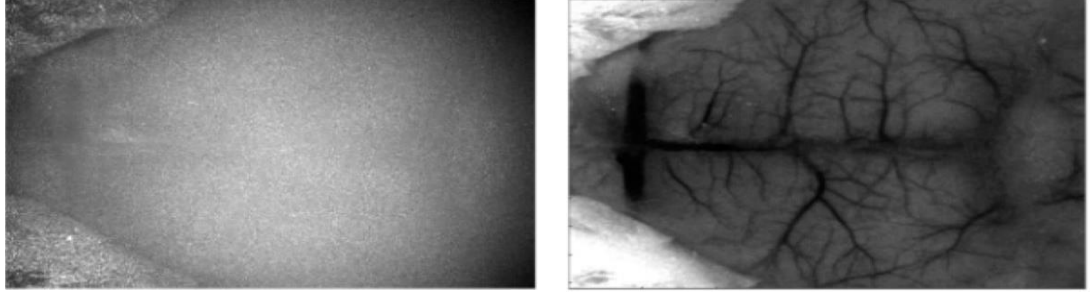
Laser speckle contrast imaging (LSCI) is a noninvasive optical imaging strategy that can provide information on the dynamics of light scattering particles. Due to the incredible spatio-temporal resolution and execution simplicity, LSCI has become a key imaging method and tool for analyzing and monitoring perfusion in organs such as the brain, skin, retina, and various others. LSCI analyzes speckle patterns and variations in them as a result of interference of coherent light scattered by light-

scattering particles, such as red blood cells. Advancement and movement of the particles cause optical power changes and fluctuations, which occur as a blurred speckle pattern when recorded by a camera with a finite exposure time. Blurring of the speckle pattern is directly associated with the particles' dynamics, and hence with the blood flow, and can be estimated as speckle contrast K . The trend of the contrast-to-flow relationship depends upon the characteristics of the light scattering process in the model, such as scattering framework (single or multiple), particle motion type (ordered or unordered), and presence of static scattering. These characteristics are depicted in the models of the intensity and temporal field autocorrelation function - $g_2(\tau)$ and $g_1(\tau)$. Under the standard assumptions of the LSCI theory, the contrast-to-flow relationship translates into $1 / K^2$ BFI, where BFI is the blood flow index. This relationship permits data processing in real time considering its numerical ease and has been likewise adopted in the vast majority of LSCI applications.

Briefly, K_s is given by:

$$K_s = \frac{\sigma_s}{\langle I \rangle} \quad (2.7)$$

where $\langle I \rangle$ and σ_s are the mean and standard deviation of the intensity in the surrounding area of a pixel. The inverse squared of speckle contrast, K_t , which is directly proportional to blood flow can also be obtained using LSCI. Figure 2.6. shows such example of the blood flow map of a rodent brain blood vessels obtained after plotting the K_t [16, 17]:



(a)

(b)

Figure 2.6: Laser speckle. (a) Typical speckle pattern obtained on rodent head, (b) Inverse of squared speckle contrast K_t , mapped demonstrating blood vessels in rodent brain. [47].

The spatial fluctuation or variance σ_s^2 and, in this manner, speckle contrast, can be connected to the intensity autocorrelation function $g_2(\tau)$ with the intensity covariance $C_t(\tau)$:

$$\sigma_s^2(T) = \frac{2}{T} \int_0^T (1 - \frac{\tau}{T}) (C_t(\tau)) d\tau, \quad (2.8)$$

$$C_t(\tau) = (g_2(\tau) - 1) \langle I \rangle_t^2, \quad (2.9)$$

where T is the exposure time, τ is the time delay. There are no presumptions related to the light-scattering process in these equations. In any case, assumptions are needed to relate $g_2(\tau)$ to the temporal field autocorrelation function $g_1(\tau)$ and consequently to the dynamics of the particles. In the original derivation, the light scattering medium was thought to be ergodic, hence permitting the utilization of the Siegert relation:

$$g_2(\tau) = 1 + \beta |g_1(\tau)|^2, \quad (2.10)$$

where β represents the loss of correlation due to the speckle averaging, polarization, and the low stability and coherence of the light source. In particular, in addition to the latest studies, the type of field correlation function $g_1(\tau)$ is generally defined as follows:

$$g_1(\tau) = \exp(-\tau/\tau_c), \quad (2.11)$$

which compares to the single-light scattering from the unordered movement of dispersing particles or to multiple-light scattering from the ordered motion of scattering particles. Combining Eqs. (2.7–2.11), this results in the equation that relates the spatial speckle contrast to the decorrelation time:

$$K = \beta^{0.5} \left\{ \frac{\tau_c}{T} + \frac{\tau_c^2}{2T^2} \left[\exp\left(-\frac{2T}{\tau_c}\right) - 1 \right] \right\}^{0.5} \quad (2.12)$$

Equation (2.12) can be solved to find the decorrelation time and obtain the estimate of blood flow in the form of the inverse decorrelation time $1/\tau_c$. However, the solution of the equation is sometimes done in practice, as it is computationally expensive and requires pre-calibration of the parameter β . Taking everything into account, to allow real-time processing and ease of adoption of the technique, the equation was further smoothed out and the blood flow index (BFI) was introduced as

an estimate of perfusion.

$$K \approx \left(\beta \frac{\tau_c}{T} \right)^{0.5} \quad (2.13)$$

$$BFI = 1/K^2 \approx \frac{1}{\beta} \frac{T}{\tau_c}, \quad (2.14)$$

This imaging technique, along with the ability of scanning non-invasively, has a high temporal resolution in the range of few milliseconds. This imaging technique is suitable to acquire data related to speckle pattern and plot the relative blood flow map, in tissue-mimicking phantoms or animal models.

2.5 Diffuse Correlation Spectroscopy

Diffuse correlation spectroscopy (DCS) is a non-invasive optical technique used to study the dynamics of a scattering (or turbid) medium by analyzing the scattering properties of coherent light [28–34]. The method works in a similar way to laser speckle contrast imaging (LSCI), which also measures laser light speckle patterns to evaluate blood flow velocity. However, DCS differs from LSCI in that it mainly measures temporal fluctuations, whereas LSCI mostly monitors spatial fluctuations.

To perform DCS, a coherent laser source generates a point source signal that penetrates into the tissue of interest. As the signal interacts with the moving red blood cells in the tissue vasculature, it is scattered and reflected. The reflected light is then detected at the tissue surface with a photodetector.

The dynamic scattering of the moving blood cells causes the detected intensity of

the reflected light to fluctuate over time. This temporal fluctuation is quantified through the intensity temporal autocorrelation function of the collected light, which provides information about the dynamics of the tissue [35]. This technique is particularly useful for investigating blood flow in deep tissue, as it is non-invasive and can be used to study tissues up to a depth of several centimeters.

The movement of the scatterers in blood cells is linked to the G1 function, which is the temporal autocorrelation function of the unnormalized electric field. The correlation diffusion equation defines this relationship [36] and is as follows:

$$(D\nabla^2 - v\mu_a - \frac{1}{3}v\mu'_s k_0^2 \alpha \langle \Delta r^2(\tau) \rangle) G_1(\vec{r}, \tau) = -vS(\vec{r}) \quad (2.15)$$

Where,

- v = Speed of light in the propagated medium,
- μ_a = Absorption coefficient of the medium,
- μ'_s = Reduced scattering coefficient of the medium,
- $D = v/(3\mu'_s)$ = Photon diffusion coefficient,
- k_0 = Wavenumber,
- $S(\vec{r})$ = Source light distribution,
- $\langle \Delta r^2(\tau) \rangle$ = Mean-square displacement of scatterers, delay time,
- τ = Delay time, through which the scatterer movement is characterized.

It has been proven that the diffusion model $\langle \Delta r^2(\tau) \rangle = 6D_B\tau$ relates to and fits the auto-correlation curves very well for human muscle [37] and brain tissue [38] where the effective Brownian diffusion coefficient D_B is a measure of the diffusion

coefficient that takes into account the effects of multiple scattering, which is the process by which particles deviate from their straight path due to interactions with other particles within the medium. By using the diffusion model to fit the auto-correlation curves with D_B , it is possible to obtain a more accurate estimate of the diffusion coefficient.

The blood flow index (BFI) is a combined term that includes αD_B , where α is a factor that takes into account the fraction of moving particles within the medium. By calculating the relative blood flow (rBF) changes compared to a baseline flow index, it is possible to determine the changes in blood flow within the tissue. This is useful for studying the effects of various physiological or pathological conditions on tissue perfusion.

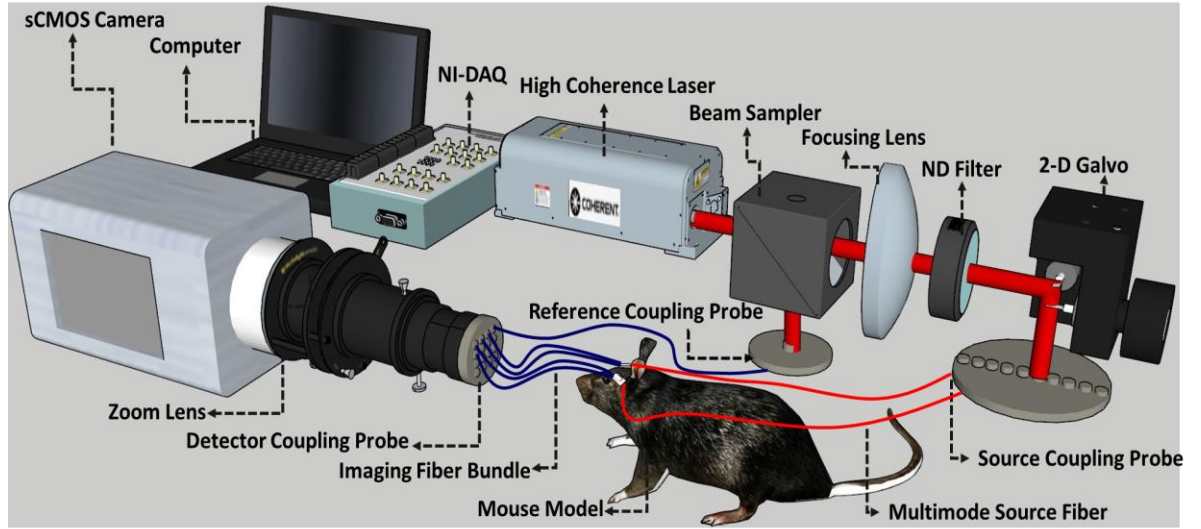
Finally, the point source and detector capability of diffuse correlation spectroscopy (DCS) enables researchers to investigate much deeper tissue than traditional methods, in the order of centimeters. This allows for a more comprehensive understanding of tissue perfusion in various organs, including the brain and muscles, which are of great interest in many medical applications.

Chapter 3 – Instrumentation

The aim of this chapter is to describe the instrument used to develop the Fiber-Camera based Laser Speckle Contrast Imaging (LSCI) setup for detecting blood flow in phantoms, and animal models. The specifications, design and their implementation are discussed below.

Figure 3.1(a) is the demonstration of the developed multi-channel Fiber- Camera based LSCI device in the form of 3D block diagram. The components which comprise the whole device are, High coherence laser, a sensitive sCMOS camera, Focusing lenses both on laser and camera side, Beam Samplers and Splitters, Neutral Density or Optical Density Filters, 1 Dimensional Galvo Scanner, Optical fibers such as Multimode fibers and Imaging Fibers, NI-DAQ, 3-D printed coupling probes for the device and the subjects, and a data collection and computing device. The most crucial components for the developed system to work are High coherence laser, a sensitive sCMOS camera, focusing lenses on camera side and optical imaging fibers.

.



(a)

Figure 3.1: (a)Block diagram of the multichannel LSCI device setup illustration various components and their interconnections

The light source being used in this device is the high coherence laser unit from CrystaLaser named DL785-100-SO. This is a turnkey laser module which is Continuous wave in nature. This diode-pumped solid state (DPSS) laser is highly stable with narrow bandwidth, low noise, low power consumption and are designed to be easy to use with a plug and play design.

This laser module comes is usually used in various medical testing applications and for various industrial settings and research purposes. This laser is highly coherent with a coherence length of > 10 m. For the application, for which this device is being developed, it requires high stability and low noise, this laser module have lower output noise (rms) of $< 0.5\%$ and good output stability of $< 1\%$, which is highly preferable for this kind of applications. This unit have an operating range of $5 - 40$ °C and warm up time of < 30 seconds, making this unit robust and quick to use in most of the clinical

and laboratory settings.

To split and focus the lasers on source and at the same time on a reference probe for power fluctuation correction, a 90:10 beam splitter is needed which transmits 90% of light intensity and reflects remaining at an angle of 90 degree. Hence in this way, both the Source and reference probe, which are at 90 degrees to each other, are illuminated at same time using same source. After being diverged due to this beam splitter, the original power output of the laser, which was around 70 mW, reduces to 63 mW and 7 mW (due to 10 % reflectance at beam splitter and 90% transmission).

The original spot of illumination created by the lasers is elliptical in shape and has a radius of 1.5 mm, which is very big to be focused on a single optical fiber for proper coupling. To counter this problem, a plano-convex focusing lens of focal length 250 mm was used to converge the focal spot of the lasers from 1.5 mm radius to 0.25 mm radius, so that it could couple with the fibers having radius 0.5 mm without much coupling losses.

The focusing lens is a plano-convex lens, which is used to converge and focus the incident light beams onto a single spot called focal point.

Also, there is another Zoom lens used at the camera side as an objective piece to collect the data, in form of received light from sample, from fibers and to focus it on the sensor of the sCMOS camera. For this application the lens had a working distance of 175 mm and has a C- mount camera montage, so it can be easily used with the camera we had. This lens had a magnification range from 0.7 to 4.5 times the original image. This specific design gives us the freedom to choose and adjust the speckle size from the fiber onto the pixels on the camera and is very suitable for LSCI applications.

ANSI standards dictates that the range of maximum permissible power output of laser for exposure of skin is in the range of 2.4 to 4 mW/mm². This power output of laser coming from the focusing lens is comparatively very high according to these standards and hence in need of attenuation. To attenuate the intensity, we used NE10A-B by Thorlabs, the OD filters of OD 1. According to the equations as stated below, where T is the transmittance, we will get intensity closer to 10 times less than the original intensity using OD filters of magnitude OD 1.

$$OD = \log_{10} \left(\frac{1}{T} \right), \text{ or } T = 10^{-OD} \quad (3.1)$$

Based on the formula above, we get the power attenuation by the factor of 10 which makes the laser power output well within the permissible range, according to ANSI standards.

To transport optical (light) signals from one location to another, optical fibers have been in use for a long time, which transports the light based on the principle called total internal reflection, which is complemented by Snell's law. Since light is being used as signal, the speed of data transmission is usually very high, which is favorable for the Laser Speckle Contrast Imaging (LSCI). This also allows the system to acquire the data at higher frequency, hence giving a chance to the researchers to analyze the frequency spectrum related components in the data as well.

Fibers are classified into different categories for different applications based on the element numbers in the core, their core size and composition. For instance, usually optical fibers are made of plastic or glass, glass being highly efficient with less losses tend to be less flexible and bulky. Based on the size of the core, fibers can be divided

into two general categories namely single mode having fiber core diameter less than 9 micrometers, few mode fibers having fiber core diameter between 9 and 50 micrometers and multimode having fiber core diameter more than 50 micrometers. For the LSCI application being discussed above, we need to transfer the speckle fluctuation of the particular location onto the detector chip, hence the suitable fiber for this application is use of imaging fiber which is a bundle of large number of single/few mode fibers clumped together in small diameter, as illustrated in figure 3.6.b. These types of fibers are also used typically for applications involving devices such as fiberscopes, endoscopes and other medical applications.

The applications being discussed require data collection from the hairy region of head of the subject and can cause higher attenuation due to hair covered region and hair roots. This discards the idea of contactless data accumulation and hence fibers are needed. Since in this application the fiber is needed to be placed on the head, the fibers need to be flexible, light weight, lower attenuation mediums and must support the ability of transporting the pixels from the surface to the detector without cross talk. Based on all the reasons stated above, it was decided to go with the multielement imaging plastic fiber, which contains 13,000 elements covering a diameter of 1.5 mm hence allowing better signal collection.

The fibers being used in the device are manufactured by Asahi Kasei. It has small transmission losses close to 1 dB per meter, based on the information provided by the manufacturing company, for wavelengths close to the range we are using. Due to the fact that these fibers are light weight and flexible, this can be used for high density multichannel scanning purposes on human or animal subjects for NIRS based

applications.

To collect optical data from sample with high quantum efficiency and lower noise, similar studies have been done in past using detectors such as simple photo diodes to highly advanced Avalanche photo diodes (APD), but these detectors have a drawback, one detector can only be used at one location causing the need of multiple detectors for multiple locations, causing the setup to be bulky, complex and very expensive. To overcome this drawback a novel approach using a camera for detector is used which can replace multiple APD detectors with one single camera. Theoretically speaking every single pixel on the camera sensor chip can be used as a single individual detector. In this setup we have used a sCMOS camera by ANDOR, which consists of 6553600 pixels which can theoretically be used as 6553600 individual detectors with just one single camera, thus eliminating the requirement of separate individual detectors for every individual location, and in the process can make the setup compact, portable, affordable, less complex and gives many advantages instrumentation wise causing the working and processing of the system much simpler.

The camera being used consists of 5.5 mega pixels and has a frame rate of 100 frames per second as rolling shutter when using with camera link and 49 fps with global shutter, for the full frame for an array size of 2560x2160 pixels. This frame rate can increase if the Region of interest is smaller than the full size of the sensor and the frame rate increases as the region of interest decreases. The frame rate of the camera is also dependent on the parameters such as type of shutter being used, exposure time, type of connectivity, number of pixels being used, binning, etc.

The sensor of this camera consists of an array of pixels which are made up of

thousands of active sensors in the form of pixels. The photons incident on these pixels are converted into electric voltages which are transmitted to other parts of chip (Analog to Digital Converter (ADC)). This effect of conversion of light energy into voltages is termed as photoelectric effect, where the energy of certain wavelength when bombarded on a particular metal surface emits certain charges in form of electrons causing the rise in potential differences which is indicator of the light photons being incident on the sensor surface and this Potential difference is directly proportional to the photons being incident on the sensor of the individual pixel on CMOS chip. This potential difference is then combined from each pixel and then output as collected and measure signal.

This camera has high dynamic range since this is a 16- Bit camera making it ideal for multiple channel data acquisition over a high range if incident photon intensity. The sensor size of this camera is $16.6 \times 14.0 \text{ mm}^2$ with pixel size of $6.5 \text{ }\mu\text{m}$. This camera has quantum efficiency of 60 % which is comparatively on higher end as compared to most other scientific cameras in the market. This camera is also equipped with different trigger options namely Internal, externa, software, etc. making the camera versatile to use. This same feature is used to trigger the camera internally to acquire data after interfacing it with MATLAB.

This camera comes with different command libraries and packages to help the user to interface this camera with different programming and data acquisition software and platforms. Amongst all the packages being provided for this product, we used Andor SDK3 which helped us to communicate and interface the camera with Matlab, which was further used to interface galvo and the camera to work together to operate and

acquire data from different source detector locations.

Chapter 4 - Device validation and results

4.1 Testing for laser stability

Output stability of the laser is an important factor to be considered in the LSCI instrumentation. As the blood flow changes being observed are small, the device needs to be sensitive enough to detect these changes. But if the laser output fluctuates over the course of the measurements, these fluctuations will result in changes in the detected flow output, which might then be considered falsely as tissue blood flow changes. Therefore, the Laser stability was measured over a span of 25 minutes to measure its standard deviation after normalizing its output with the initial value. A liquid phantom made from intralipid and Indian ink, having optical properties of absorption parameter 0.1 cm^{-1} and scattering parameters of 10.0 cm^{-1} at wavelengths 785 nm respectively, was used. Shown in Figure 4.1. are the normalized results. The percentage standard deviation for the laser was 0.0628. The standard deviation is low enough to not have a significant effect on intensity change calculations or on the blood flow changes calculation.

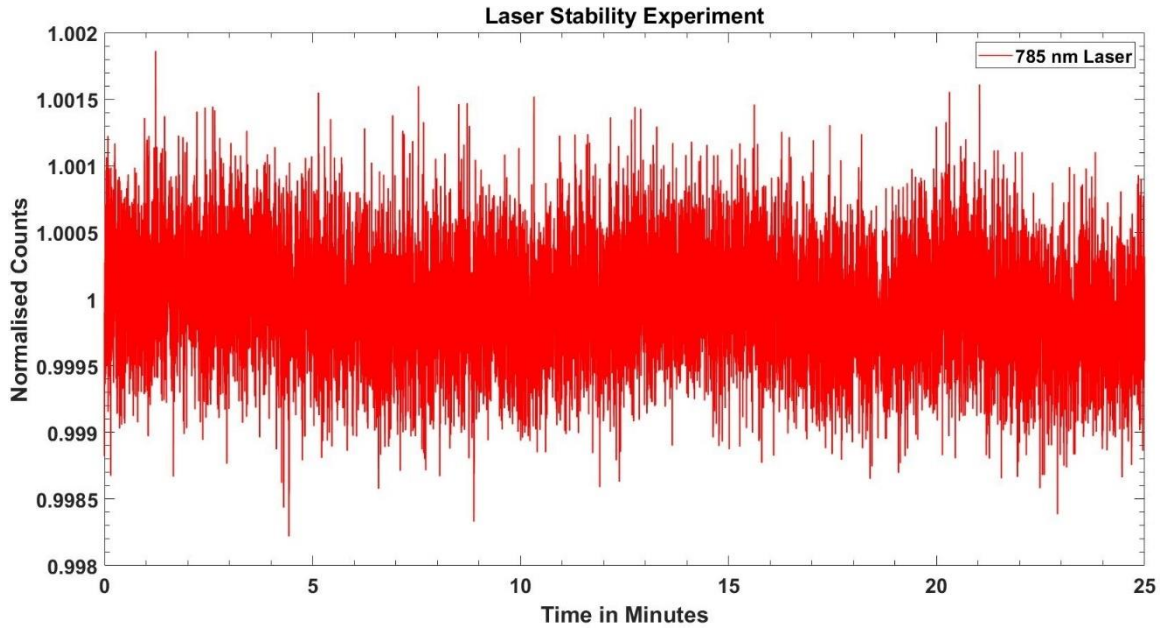


Figure 4.1: Plots of the results of the laser power stability testing over 25 minutes.

4.2 Signal – to – noise ratio (SNR) testing

To quantify the measurement sensitivity of developed sCMOS based LSCI imaging system, a liquid phantom with absorption coefficient 0.1 cm^{-1} and scattering coefficient 10 cm^{-1} , at 785 nm, was used (made using Indian Ink and Intralipid). The distance between source – detector fibers ranged from 1.8 to 3 cm. The integration time for sCMOS was varied between 1 to 20 ms. The actual signal acquired was average to get the signal intensity. To get the noise, the standard deviation of the background noise was taken when the laser was off. Then, the ratio of signal to noise was calculated to obtain SNR.

The calculated SNR measurements for wavelength 785 nm for the fiber camera setup is presented as in Fig.4.2.1. We can see that the SNR is decreasing strongly as a function of distance.

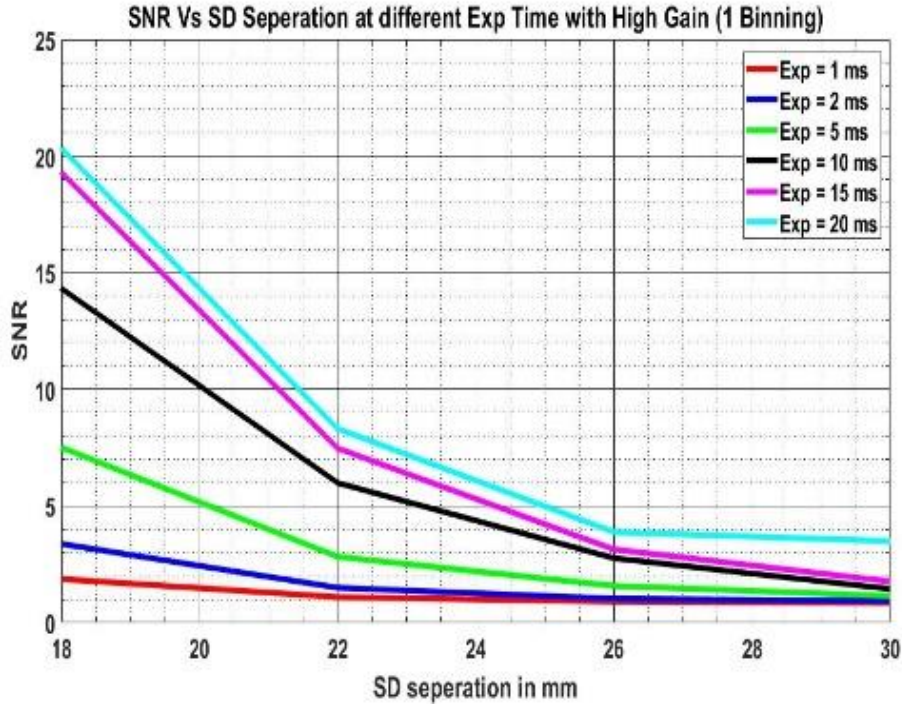


Figure 4.2.1: Results of SNR as function of SD separation.

The SNR of the camera is calculated using the formula as follows.

$$SNR = \frac{QE * S}{\sqrt{F_n^2 * QE * (S + I_b) + (N_r/M)^2}}$$

This equation gives the relation of SNR with respect to the signal or counts, where,

QE = Quantum efficiency (0.55 for 785 nm),

F_n = Noise factor (1.44 in our sCMOS),

I_b = Background counts,

S = Input signals,

N_r = Readout noise (2.4 for this case for global shutter (at 560 MHz readout rate)),

M = Electron multiplying (EM) gain (1 for sCMOS),

N_d = Dark noise (assumed to be zero) [110, 111].

Quantum efficiency is the ability of a camera to convert incident photons into photoelectrons. This is dependent on wavelength. SNR is directly related to QE.

Readout noise is the measure of fluctuations of the photoelectrons which converts the charge of photoelectrons from each pixel to its related digital number expressing its intensity.

Dark noise is the noise generated due to thermally generated electrons which are results of heat generated by the camera. This noise is time and temperature dependent. Since most of the cameras are equipped with cooling fans and they operate at very low exposure time, this noise may be low.

Signals here are the average of the signal counts acquired over a time specific time. Similarly, background signal is also averaged. Sometimes the background signals can contaminate the real signal hence it is important to take the background signals into consideration [111]. All the above values are taken from the Hamamatsu Orca 4.0 sCMOS camera datasheet [110].

Calculating and comparing the SNR data of the ideal and actual cameras, we get results as illustrated in Figure 4.2.2

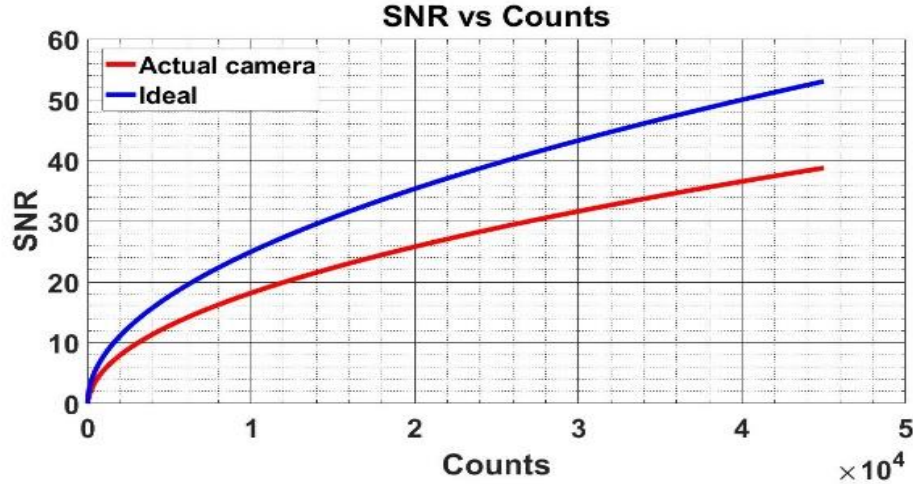


Figure 4.2.2: SNR with respect to counts for both ideal camera and sCMOS.

4.3 Dynamic Flow Phantom linearity testing

To determine systems sensitivity and accuracy in detecting small changes in the flow, and to quantify the changes accurately, the dynamic flow phantom linearity testing experiment (in reflectance configuration) was performed. A hollow tube filled with glass beads was embedded inside a solid scattering phantom body. The tube was buried 6 mm underneath the phantom surface. Intralipid solution with a small concentration of Indian Ink (To mimic optical properties in living tissue) was pumped through the tube using a syringe pump. This tissue mimicking liquid phantom was made with absorption coefficient 0.1 cm^{-1} and scattering coefficient 10 cm^{-1} with the help of intralipid (Intralipid 20% by Fresenius Kabi) and Indian Ink. The schematic of the experimental setup is shown in Fig. 4.3.(a). A long-coherence 785-nm laser (CrystaLaser) was used as the light source and a sCMOS camera (Orca-Flash 4.0 from Hamamatsu) was used as the detector. A fiber bundle with a core size of 2 mm with individual element 15-micron diameter and approximately 17,000 number of elements

(Schott) was used as the detector fiber, and a multimode 600-micron core size fiber (OZ-Optics) was used as source fiber to deliver the laser light into the phantom. One end of the detection fiber was placed on the surface of the phantom, and the other end on the camera side. An exposure time of 1 ms was used and the S–D separation was 15 mm for the phantom experiment. 100 images were acquired in each case for different flows and also to generate the background intensity profile for background correction. Every acquired frame was corrected against the averaged background intensity. An area of 200×200 pixels of the corrected speckle pattern was used for $1/K^2$ calculation, as indicated by the highlighted square box in Fig. 4.3(a).

As shown in the results of figure 4.3(b). flow data was acquired at different flow rates and 100 images were taken, processed, averaged, and plotted to get a good linear relationship between the pumping speed and the calculated flow measurement. In the figure below, the solid line is the calculated flow with respect to the pump speed, and the dotted line is the linear fit estimation based on the calculated. The R^2 values observed were approximately 0.95 which shows a high linear relationship of $1/K^2$ vs pumping speed, which is expected. This indicates that the linear equation and the actual data plotted are highly co-linear, hence it proves that the system works perfectly and quantifies data accurately.

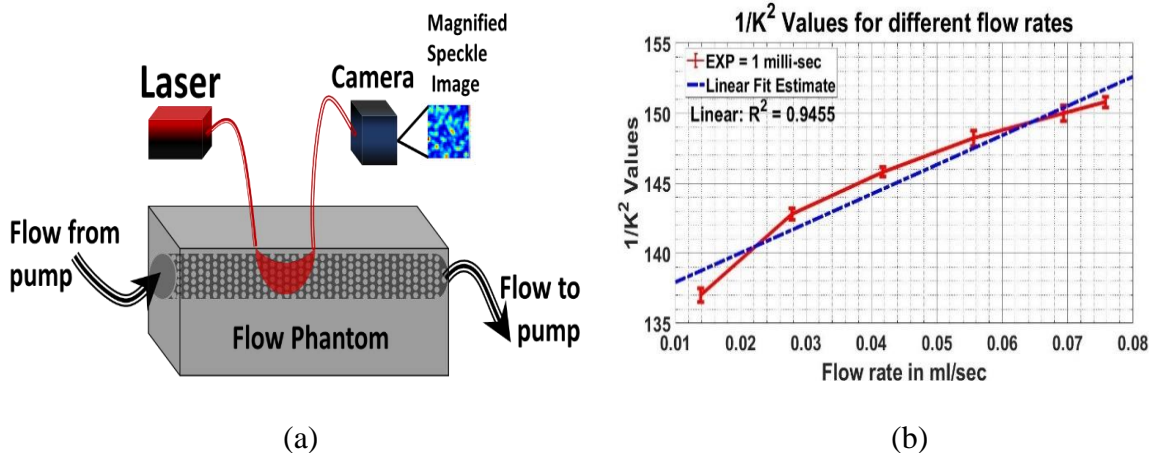
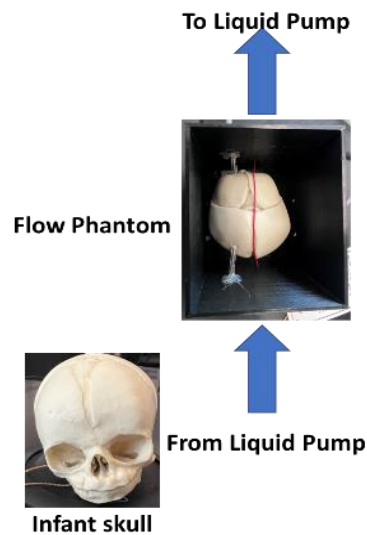


Figure 4.3: (a) Schematics of the flow phantom experimental setup for Fiber-Camera LSCI system. (b) Averaged Flow measurement at each flow rate.

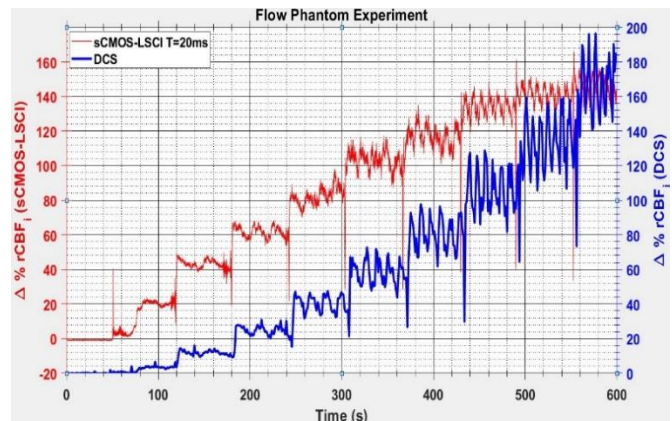
4.4 Human Infant Head Mimicking Phantom

To further prove and test the hypothesis that this device works well and quantifies data and CBF, in living tissue mimicking model was made. This model consisted of an artificial infant-mimicking skull, a tube mimicking the artery, and a layer of liquid phantom consisting of water, intralipid and Indian ink, with absorption coefficient 0.1 cm^{-1} and scattering coefficient 10 cm^{-1} , to mimic the optical properties of the scalp layer on the head. The tube is situated 0.6 cm deep within the phantom, which was pumped through the tube by a syringe pump to mimic intracerebral blood flow. The schematic of the experimental setup is shown in Fig. 4.4.(a). An exposure time of 10-20 ms was used and the s-d separation was 13 mm for the phantom experiment. 100 images were acquired in each case for different flows and also to generate the background intensity profile for background correction. Every acquired frame was corrected for the averaged background intensity. An area of 200×200 pixels of the

corrected speckle pattern was used for $1/K^2$ calculation. To further validate the system, the developed system was compared with the lab standard device and method called Diffuse Correlation Spectroscopy (DCS), which was used to take readings of the flow simultaneously with the developed Fiber-Camera LSCI device. The flow was varied from 0 to 10 ml/sec over a span of 10 minutes. The percentage change in the mimicked relative Cerebral Blood Flow (rCBF) in both the developed Fiber-Camera system and the DCS is linearly proportional to the change in flow velocity being changed over the period of time, as shown in Fig. 4.4.(b). The readings from both the devices aligned well with each other demonstrating the capability of the developed device compared to “lab-standard”.



(a)



(b)

Figure 4.4: (a) Schematics and model of the flow phantom experimental setup for Fiber-Camera LSCI system in a phantom mimicking human infant head. (b) Averaged Flow measurement at each flow rate and comparison with DCS.

4.5 Muscle blood flow occlusion experiment

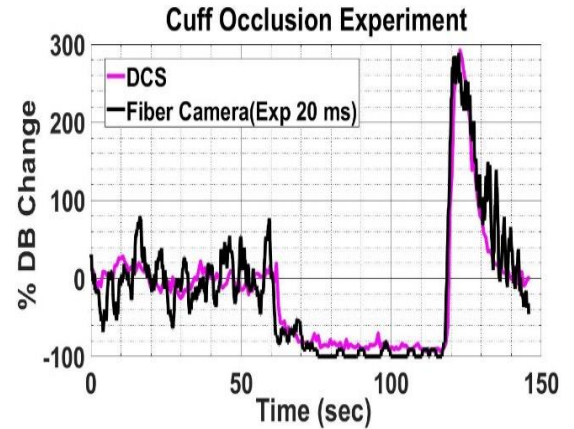
Next, the device was tested on a human arm. This experiment was performed to check if the device is able to quantify and detect the blood flow changes accurately to observe and record the expected trend in similar well-established occlusion protocol for *in-vivo* cases [68,62,73,74,75]. For this experiment, one healthy male of age 28 was selected as a volunteer. The arm occlusion experiment described above shows the following results as described in figure above. It follows a baseline for 1 min when there was no pressure applied. After 1 min the blood flow is cutoff and starts decreasing as arm was occluded. After 1 min as pressure was released, there is sudden rise in blood flow, causing an overshoot in the blood flow gradually approaching back to baseline, which can also be called autoregulation of blood flow.

A standard arm occlusion test was performed, as shown in figure 4.5(a). A pair of source and detector with S-D separation 2.5 cm was strapped to a human arm and the pressure cuff was attached to the upper arm of the subject. The exposure time for sCMOS was 20 ms here. The first 1-minute no pressure or perturbation was applied (baseline was observed). Then, a pressure of 220 mmHg was applied to the arm, occluding the blood flow. This would prevent venous and arterial blood flow from and to the forearm. In this process, the expected trend is a complete cutoff of circulation in blood flow causing drop in blood flow rapidly. The data was then collected for 1 min. Then the pressure was released, and the data was collected for 1 minute. In this process the blood rushes into the arm. Here, the expected trend is sudden rise and overshoot in blood flow which then settles to go back to baseline. The results were compared to Diffuse Correlation Spectroscopy (DCS) system as a lab standard and the developed

Fiber-Camera LSCI system did show similar results, as shown in figure 4.5(b), thus validating the developed system in human arm.



(a)



(b)

Figure 4.5: (a) Experimental setup of arm occlusion experiment. (b) Relative Blood Flow Results obtained for arm occlusion test for the single channel camera system and compared with a single-channel DCS.

4.6 Muscular Dystrophy Disease Mouse Model

After confirming the working of the developed device on artificial flow mimicking phantoms, for the next phase, the muscle stimulation experiment and the blood flow measurement corresponding to that stimulation were done on the animal model. A preliminary study was conducted on the Double Knockout genetically treated mouse model for Muscular Dystrophy and C57BL/6 (Wild type or control) mice were used as control sample space for mice. A sample space of $n = 5$ each for Control and Muscle Dystrophy mice was used for this study. The goal here is to differentiate the blood flow autoregulation capability of the control population and the reduced blood flow autoregulation capability of mice suffering from Muscular Dystrophy with an

observed change in blood flow rate. DCS point source imaging was used, as a lab standard along with the developed sCMOS -LSCI system, to monitor changes in BFI after repeated tetanic contractions in the mouse model.

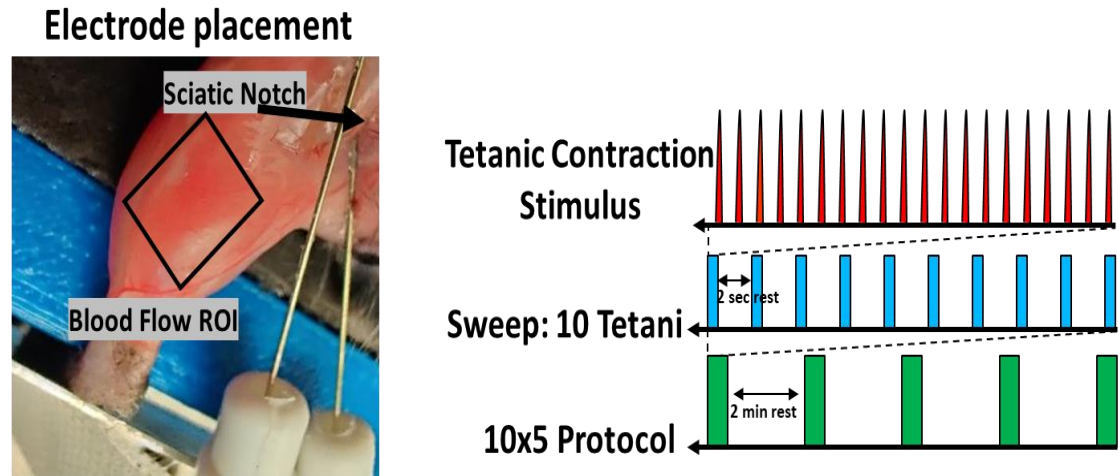


Figure 4.6: Experimental setup and the stimulation signal description for Tetanic contraction stimulus in muscle Dystrophy mouse model.

Before proceeding to the experiment, the mice were prepared for the procedure. Each animal was anesthetized using an isoflurane vaporizer unit. 5% Isoflurane was used while the oxygen flow to the anesthesia chamber to the mice is 300 ml/min. After mice were anesthetized and unconscious, they were placed under 2.5% Isoflurane and a nose cone was attached to their head, to maintain the unconscious state of the mice, while shaving their leg and thigh hair for experiment preparation for better contact of the optical probe with the leg muscle. During the whole experiment, the mice were placed on the heating pads that were made sure to be at $\sim 36^{\circ}\text{C} \pm 2^{\circ}\text{C}$.

Nerve-evoked contractions were stimulated with platinum electrodes resting on the sciatic nerve as indicated in Figure 4.6. Direct muscle contractions were stimulated

using platinum electrodes placed above and below the plantar flexor muscles. Stimulus amplitude and the pulse width was ≤ 5 V at 1 ms for nerve stimulated and muscle-stimulated contractions, respectively. A repeated stimulation protocol was developed that consisted of sweeps of 10 tetani to study muscular fatigue and the response to blood flow due to repeated contractions. The nerve was stimulated with 20 pulse trains at 30 Hz. Stimulus amplitude and the pulse width were ≤ 5 V at 1 ms. Sweeps of 10 trains were stimulated with 2 seconds between trains. There was two minutes of rest between sweeps, and five sweeps were performed in total. The whole protocol consisted of five sweeps with 10 trains at 30 Hz. From now on, this protocol will be referred to as a 10x5 repeated tetani protocol. The 10x5 repeated tetani protocol was immediately followed by rest until the 25 min time point is reached. The source-detector separation was reduced to 5 mm to ensure that most of the detected photons traveled through the belly of the leg muscle being stimulated.

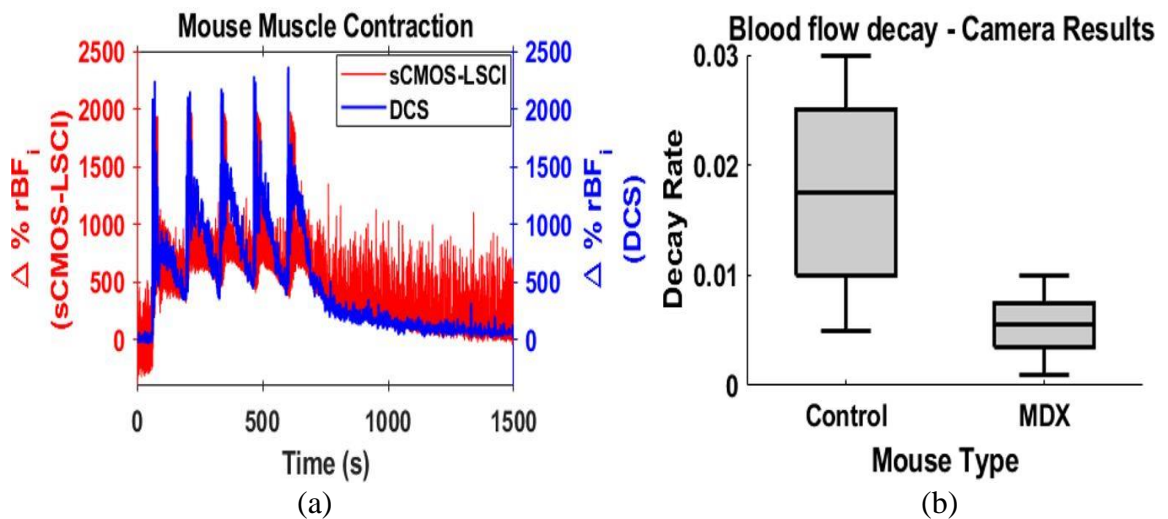


Figure 4.7: (a) Relative Blood Flow Results obtained from control mouse for the experiment for single channel and comparison with DCS. (b) Wilcoxon rank-sum test of the slope of decay of relative muscular blood flow after stimulation of control and Muscular Dystrophy mice group to see the significant difference in the magnitude.

Figure 4.7(a) indicates the relative blood flow index calculated by the developed system as well as the lab standard DCS system. There is almost no change in the blood flow during baseline, during perturbation (Stimulations) blood flow tends to increase due to contraction of muscle and during rest, the blood flow tends to come back to baseline. As observed from the results, peaks keep rising with each cycle of stimulations, and after last stimulation, blood flow try to go back to baseline (autoregulation), which is expected from healthy and genetically treated mice. As it can be observed, the results of camera-based system and the lab standard system are closely aligning well, and the advantage of the developed camera system is higher acquisition speed which can be seen from the time-course results.

After finding the slope of the decay of relative muscular blood flow in mice after the stimulation, using the single exponential fit, for a sample of 5 mice belonging to each group, Wilcoxon rank-sum test, as demonstrated in figure 4.7(b), was performed to find the differences in the slope of decay of these two groups. It was found out that there is significant difference between the slope of recovery in muscular blood flow in the two groups with very high P value of $p = 0.0011$, suggesting that the control mice recover muscular blood flow quicker than the diseased Muscular Dystrophy mice model. This states that the developed device can successfully distinguish the control mice from the diseased mice based on the muscular blood flow.

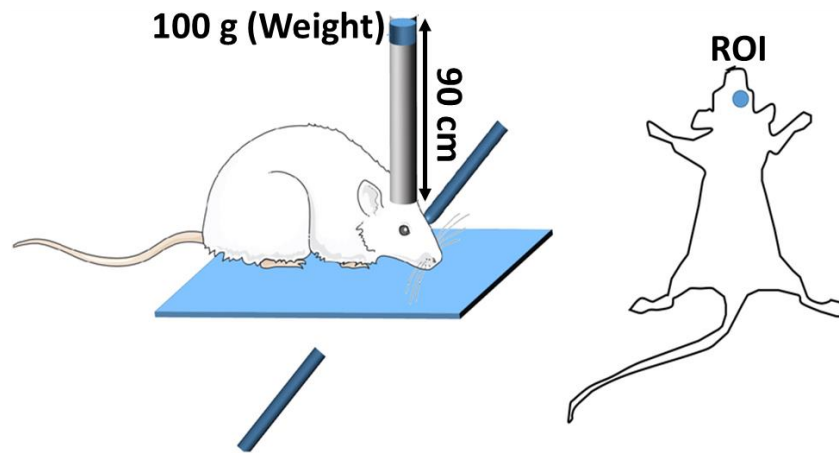
4.7 TBI Mouse Model Experiment

Optical imaging is useful for quantifying both function and structural information in vivo. Functional information includes blood oxygenation, blood flow, blood volume,

cellular metabolism, tissue scattering and fluorescence via optical spectroscopy. Structural information includes depth/thickness of lesions, location of bones/organs and tissue macro/microstructures via optical tomography. By combining these techniques, it is possible to co-register both structural and functional information for better understanding the presence, progression, and response to treatment of a disease or condition. During the onset and progression of traumatic brain injuries, there are often structural and functional changes. For localized conditions, there will be a difference between the affected area and the surrounding "normal" area. This can be used to indicate the presence of a condition as well as the severity. In addition, as conditions progress there will be changes from the initial levels, which may provide information about the progress of the condition or the response to treatment. To prove the same hypothesis stated above, a mouse model for inducing Traumatic Brain Injury (TBI) was used and the cerebral blood flow was measured afterwards to see and differentiate the effects of injury on blood flow.

In this study, we are using 10 female C57BL/6J mice which are ~12 weeks old and weigh ~ 40 grams. The mice were kept and cared for in the department of Laboratory Animal Resources (LAR), the animal facility, where they were given free access to food and water, maintained at $23 \pm 2^{\circ}\text{C}$, and placed under a 12-h reverse light/dark cycle. Each animal was anesthetized using a isoflurane vaporizer unit. 5% Isoflurane was used while the oxygen flow to the anesthesia chamber to the mice is 300 ml/min. The depth of anesthesia was sufficient enough for mice not to notice the withdrawals from the toe pinch. After the mouse was anesthetized, mice were placed under 2.5 % Isoflurane and nose cone was attached to their head, to maintain the unconscious state of mice, while

shaving their scalp hair for experiment preparation. The mice are then placed back in their respective colony room for one day. Next day for the experiment the mice were anesthetized again in the anesthesia chamber using 5 % Isoflurane and then switched to 2.5 % Isoflurane for rest of the experiment. During this whole experiment, the mice are placed on the heating pads which were made sure to be at $\sim 36\text{ }^{\circ}\text{C} \pm 2^{\circ}\text{C}$.



TBI Mouse Model

Figure 4.8: Experimental Setup representing the Traumatic Brain Injury module in mice.

First, before inducing any injury in mice, the control measurements were recorded and calculated to ensure the proper working of the device and to ensure that the baseline of $\sim 0\%$ change in blood flow is obtained. After the control measurements were taken, for comparison with induced brain injury blood flow changes, the setup was made for TBI induction in mice. For inducing the brain injury and causing TBI in the mice, we adapted the weight drop technique, as shown in figure 4.8, in which a cylindrical metallic weight of 100 grams was dropped from a height of 90 cm above the mouse

head. Immediately after the weight was dropped and the injury was induced on mouse head, the mouse was transferred to the optical setup platform where the optical measurements are being recorded for 30 mins. This entire duration, the animal was anesthetized, and as soon as the 30 mins measurements stopped, the mice were euthanized using the cervical dislocation technique, so that no significant painful events occur during the entire period.

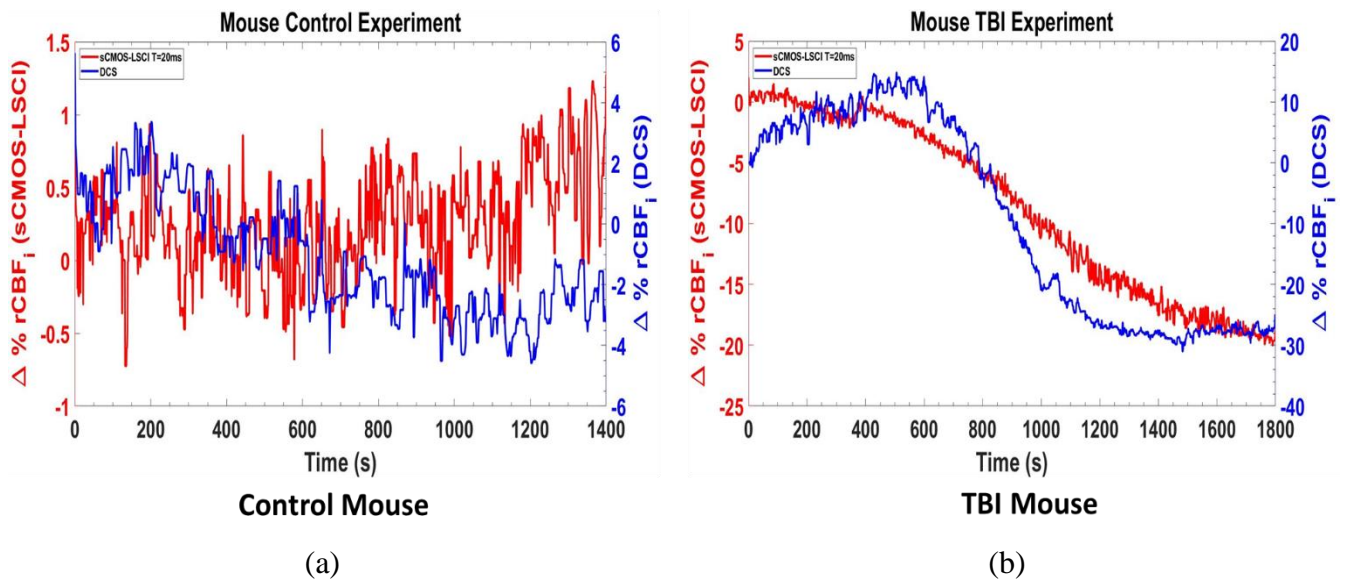


Figure 4.9: (a) Relative cerebral blood flow results of one control mouse experiment. (b) Relative cerebral blood flow results of one mouse after TBI was induced.

The results of the above experiment are plotted later as can be seen in figure 4.9. In the mouse classified as control, no injury was induced, and the mouse was anesthetized and was in resting condition for entire duration. As seen in the results in figure 4.9(a), there is no significant change in the relative blood flow and the relative mean blood flow is $\sim 0\%$. In figure 4.9(b), the results are plotted for the measurements of post TBI, in the results it can be seen that the blood flow drops significantly and rapidly after the cerebral injury was induced. The blood flow drops rapidly for the entire

duration of 30 minutes of measurement as compared to the control case where there is no significant relative change.

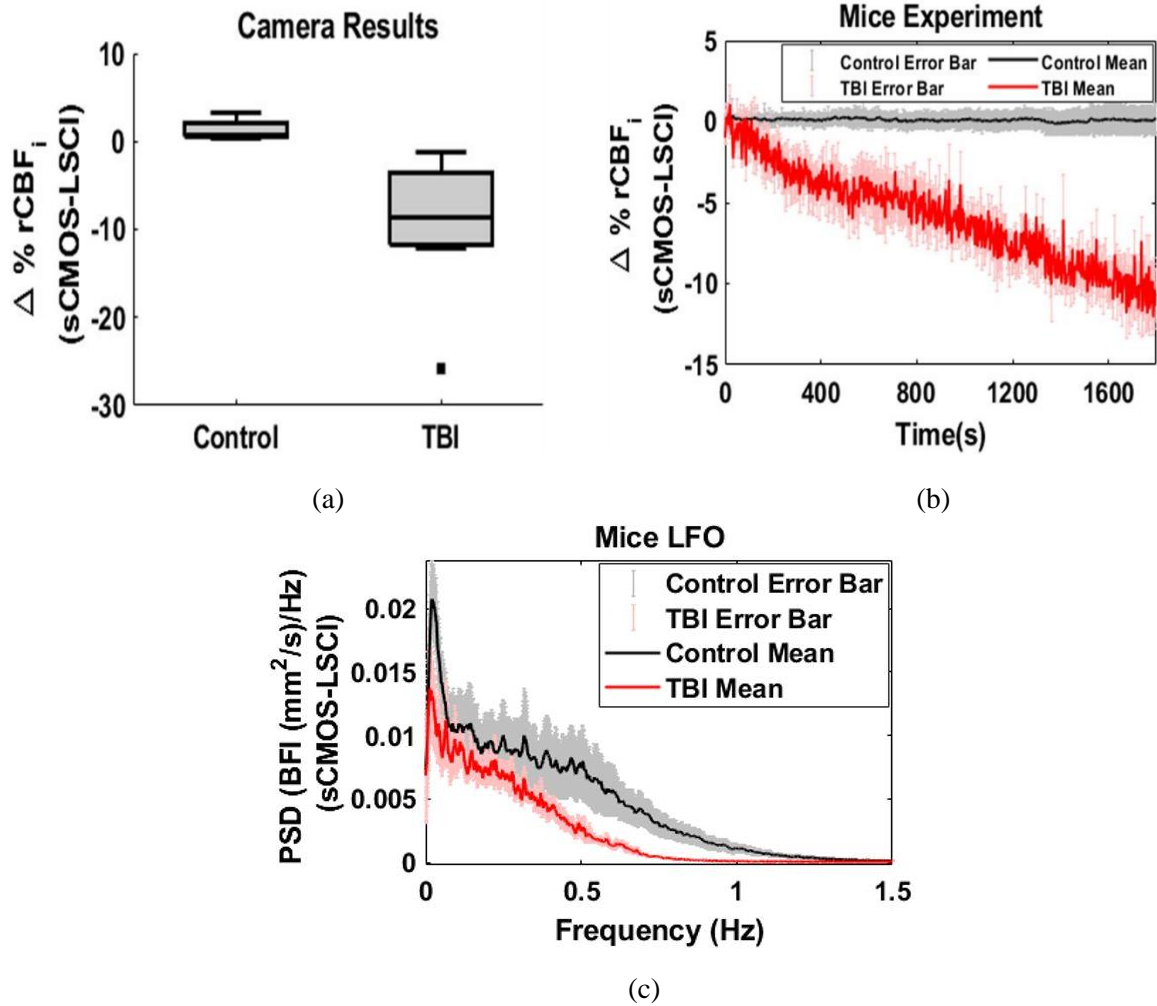


Figure 4.10: (a) Wilcoxon rank-sum test of the relative CBF of control and TBI mice group to see the significant difference in the magnitude. (b) Mean and standard error of relative CBF of all the control and TBI induced mice. (c) . Mean and standard error bars of frequency spectrum of CBF for 10 control and TBI mice each.

The same experiment was performed for $n = 10$ mice. Control and TBI results were plotted and, as seen in figure 4.10, Wilcoxon rank-sum test was performed and plotted to compare the statistical significance difference between the magnitude change of cerebral blood flow between TBI and Control mice. It was observed that the mean of

relative blood flow changes of Control mice was ~ 0% and the mean of relative blood flow changes of TBI mice was ~ 10% after 30 mins. As seen in the figure 4.10 (a), it can be seen that there is clear statistical and significant difference between both the cases, with a p-value $p = 4.1135 \times 10^{-5}$. This states that there is a very strong and significant difference between relative blood flow of TBI and Control population, and this device is capable of detecting that change and differentiating Control patients from TBI patients. Figure 4.10 (b) indicates the averaged trace of percentage change in relative cerebral blood flow for both control and TBI mice model. It can be clearly seen that there is a significant difference between the control and the TBI mice model rCBF after 30 mins of impact, and this condition is highly repeatable hence proving the case and the capability of the developed device to differentiate between the control and TBI population and also the severity of TBI with its localization. Figure 4.10 (c) displays the mean and standard error of frequency responses for 10 mice in each group, namely the control and TBI population. The graph depicts the low frequency oscillation in the frequency response. A comparison between the results of the control and TBI mice reveals that both groups have similar-shaped frequency responses. Notably, both groups display significant activity in the range of 0.01-0.06 Hz, and there is a smaller yet noticeable response beginning approximately 0.24 Hz onwards. Furthermore, the PSD of TBI mice population is around 0.014 ((mm²/s)/Hz) at 0.02 Hz, while for the Control population, it is around 0.021 ((mm²/s)/Hz). These findings are consistent across all 10 mice in each group, as demonstrated by the standard error displayed in figure 7. Additionally, there are visible significant differences in the PSD throughout the frequency range, particularly from 0.4 Hz to 1.15 Hz. These results suggest that the LFO

metric may serve as an effective tool to compare a mouse's normal functioning frequency response with their diseased response on an individual level. Therefore, the LFO metric could potentially aid in identifying specific abnormalities in frequency response and assessing the efficacy of treatments for TBI.

4.8 Towards Human Brain Measurements

As for the future direction, I have tested the sensitivity in human heads by using standard head of bed (HOB) experiment. For this experiment we picked a healthy 28-year-old male volunteer, the same as the muscle blood flow occlusion experiment. In this experiment the subject had an optical probe with Source-Detector (SD) separation of 2.5 cm attached to left side of Dorsolateral Prefrontal Cortex (DLPF). One source and one detector consisting of one channel for the camera-based system was used along with DCS consisting of similar configuration in the same area. Once the sensors were placed on the subject, the subject was asked to sit on the bed at 60-degree elevated position for 5 minutes to acquire the baseline. Then the bed was lowered to a zero-degree angle at a rate of 2.5 degrees per second and recording continued for five more minutes. Figure 4.11(a) below outlines both the phases of this protocol.

After the data collection, the data was analyzed and plotted. During the baseline, the blood-flow was lower as compared to the blood flow of later half of experiment, which is due to the rush of blood flow due to removal of elevation of head. The results of the camera-based system and the lab-standard DCS system are very closely correlated as seen in figure 4.11 (b), thus the results indicate that with this approach may be used on adult human head. However, the main challenge is that this is still a one-channel

system, and there is a need for improved sensitivity for appropriate scaling for multi-channel with sufficient sensitivity, which may be further investigated in the future works, as discussed below.

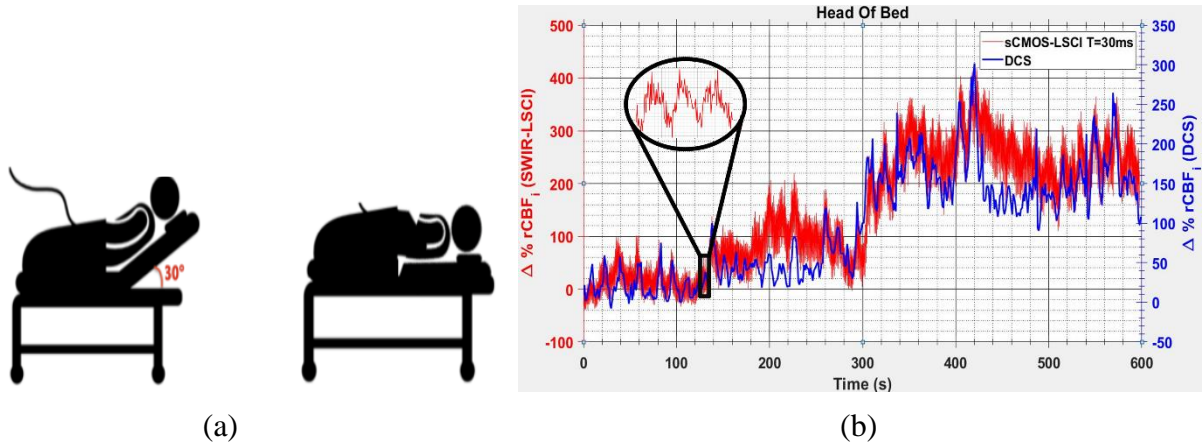


Figure 4.11: (a) Experimental setup for Head of Bed Experiment. (b) Relative Blood Flow Results obtained for the experiment for single channel and comparison with DCS

Chapter 5 - Conclusions and Future works

The chapter below will describe the results of the experiments performed using the developed device and its setup, and the results will be interpreted and concluded. Future work and directions will also be discussed in the coming chapter.

5.1 Conclusions

A one or two-channel Continuous wave Laser speckle Contrast Imaging device was developed, and the device was rigorously tested using different experiments with the help of phantoms and animal and human models.

The optical devices are capable of being mounted on a portable moving station making it mobile and portable. The developed approach is noninvasive, does not involve ionizing radiation. This is a significant advantage over the traditional functional brain imaging devices such as CT, MRI, PETs, etc. for the constructed device is also portable, potentially scalable for multi-channel for imaging applications in the future. Thus, the approach may be used for the bedside neuromonitoring applications in the future.

Apart from being used as a standalone device, it can also be used for multimodal imaging studies. such as MRI. Based on the functionality and ease of use of this device, it can find use in various application and fields and also professions such as bed side

monitoring of patients, assessing the TBI or concussions in soldiers, athletes, and human performance assessments for different research purposes. This device can be useful for bedside monitoring, for adults and neonates at neurointensive care units. This device is comparatively cheap, hence it can be used in underdeveloped countries which cannot afford the expensive devices. This device demonstrates sufficient SNR for SD separation as large as 3 cm. The SNR could be increased by reducing the SD separation or by increasing the exposure time of camera.

Despite different test mouse subjects with differing weights and ages, the results generated for the change in blood flow for control and Post TBI case had a similar trend. similar. These results reflect the pathophysiology of the brain following trauma, as investigated from a range of different methods. Taken together, this study demonstrates the potential for a noninvasive, quantitative tool for monitoring brain hemodynamics following injury.

5.2 Future works

In the future, it is desirable to further investigate for human translation. The results indicated sufficient signal-to-noise ratio when used with source-detector separations of as high as 2.5 to 3 cm, which can probe ~1 to 1.5cm depth in humans. Thus, it may be used for studying brain and muscle.

To further improve the efficiency of the device, we suggest using an optical switch to replace the 1D galvo used for scanning the source array. The optical switch would reduce the loss of light coupling in the fiber and laser source interface, which can lead to slightly more signals. But the main challenge is in the detector side, there

is a need for newly developed cameras such as single photon counting cameras.

To ensure that the device can be used effectively on people of different head sizes, the head gear that holds the optodes in place needs to be designed appropriately. This is because the distance between the optodes and the scalp, referred to as the source-detector separation, is critical for accurate scanning and imaging of functional response. A better head gear design can accommodate different head sizes while maintaining a consistent source-detector separation and optode position, which ensures that the device can produce accurate results, regardless of the user's head size.

Furthermore, the device can be made more portable and versatile by making it wireless. This would be achieved by using wireless transmission and reception modules. The wireless feature would make the device more compact, convenient, and easy to carry around. The device could then be used for field activities, exercises, or other outdoor events. Also, cameras of smaller size can be used to avoid the consumption of power, eliminating the need for a big power supply battery, also improving the portability of the device. Overall, the suggested improvements and enhancements to the device have the potential to significantly increase its imaging capabilities and expand its potential applications in various fields, including medical research and clinical diagnostics.

Bibliography

1. Zaninotto, A.L.C.; Costa, B.T.; Ferreira, I.S.; French, M.; Paiva, W.S.; Fregni, F. Traumatic brain injury. In *Neuromethods*; Humana Press Inc., 2018; Vol. 138, pp. 105–138.
2. Amyot, F.; Arciniegas, D.B.; Brazaitis, M.P.; Curley, K.C.; Diaz-Arrastia, R.; Gandjbakhche, A.; Herscovitch, P.; Hinds, S.R.; Manley, G.T.; Pacifico, A.; et al. A Review of the Effectiveness of Neuroimaging Modalities for the Detection of Traumatic Brain Injury. *J. Neurotrauma* 2015, 32, 1693–1721.
3. Le Roux, P.; Menon, D.K.; Citerio, G.; Vespa, P.; Bader, M.K.; Brophy, G.M.; Diring, M.N.; Stocchetti, N.; Videtta, W.; Armonda, R.; et al. Consensus Summary Statement of the International Multidisciplinary Consensus Conference on Multimodality Monitoring in Neurocritical Care. *Neurocrit. Care* **2014**, doi:10.1007/s12028-014-0041-5.
4. Foreman, B.; Ngwenya, L.B. Sustainability of Applied Intracranial Multimodality Neuromonitoring After Severe Brain Injury. *World Neurosurg.* **2019**, 124, 378–380, doi:10.1016/j.wneu.2019.01.047.
5. Kenney, K.; Amyot, F.; Haber, M.; Pronger, A.; Bogoslovsky, T.; Moore, C.; Diaz-Arrastia, R. Cerebral Vascular Injury in Traumatic Brain Injury. *Exp. Neurol.* **2016**, 275, 353–366, doi:10.1016/j.expneurol.2015.05.019.
6. Selb, J.; Wu, K.-C.; Sutin, J.; Lin, P.-Y. (Ivy); Farzam, P.; Bechek, S.; Shenoy, A. Prolonged monitoring of cerebral blood flow and autoregulation with diffuse correlation spectroscopy in neurocritical care patients. *Neurophotonics* **2018**, 5, 1, doi:10.1117/1.nph.5.4.045005.

7. Langri, Dharminder Singh. *Monitoring Cerebral Functional Response using sCMOS-based High Density Near Infrared Spectroscopic Imaging*. 2019. Wright State University, Master's thesis. *OhioLINK Electronic Theses and Dissertations Center*, http://rave.ohiolink.edu/etdc/view?acc_num=wright1558610822306817.
8. M. Papademetriou, "Multichannel Near Infrared Spectroscopy to monitor cerebral oxygenation in infants and children supported in extracorporeal membrane oxygenation (ECMO)", PhD. Thesis, University College of London, 2011
9. M. Cope, "The Application of Near Infrared Spectroscopy to Non Invasive Monitoring of Cerebral Oxygenation in the Newborn Infant", PhD Thesis, Department of Medical Physics and Bioengineering, University College London, 1991
10. Kim, M. N. (2013). Applications of hybrid diffuse optics for clinical management of adults after brain injury.
11. G. Brant, "Studies on lipids in the nervous system with special reference to quantitative chemical determination and topical distribution", *Acta. Physiol. Scand. Suppl.*, 18 Suppl 63, 1949.
12. Cheong, W., Pralh, S., & Welch, A. 1990. A review of the optical properties in biological tissues. *IEEE Journal of Quantum Electronics*, 26, 2166-2185
13. Dias, D. D. S. (2015). *Design of a low-cost wireless NIRS system with embedded Linux and a smartphone interface* (Doctoral dissertation, Wright State University).
14. Emily J. Rue ; Ruikang K. Wang ; Yappa A. Wickramasinghe; New four-channel continuous wave near-infrared spectroscopy device for regional cerebral oxygenation monitoring. *Proc. SPIE 3911, Biomedical Diagnostic, Guidance, and Surgical-Assist Systems II*, 218 (May 3, 2000); doi:10.1117/12.384905.

15. Draijer M;Hondebrink E;van Leeuwen T;Steenbergen W; “Review of Laser Speckle Contrast Techniques for Visualizing Tissue Perfusion.” *Lasers in Medical Science*, U.S. National Library of Medicine, <https://pubmed.ncbi.nlm.nih.gov/19050826/>.
16. Boas, David A, and Andrew K Dunn. “Laser speckle contrast imaging in biomedical optics.” *Journal of biomedical optics* vol. 15,1 (2010): 011109. doi:10.1117/1.3285504
17. Kalchenko, V., et al. “[PDF] a Robust Method for Adjustment of Laser Speckle Contrast Imaging during Transcranial Mouse Brain Visualization: Semantic Scholar.” *Photonics*, 1 Jan. 1970, <https://www.semanticscholar.org/paper/A-Robust-Method-for-Adjustment-of-Laser-Speckle-Kalchenko-Sdobnov/50b96cd8896b03c97538e971c2f9f9ddfa6a938f>.
18. Valdés Escobar, Claudia Patricia. “New Laser Speckle Methods for in Vivo Blood Flow Imaging and Monitoring.” *Pàgina Inicial De UPCommons*, Universitat Politècnica De Catalunya, 14 Jan. 2015, <https://upcommons.upc.edu/handle/2117/95584>.
19. JD Rigden and EI Gordon. Granularity of scattered optical maser light. In *Proceedings of the Institute of Radio Engineers*, volume 50, page 2367, 1962. bibliography 157
20. L Allen and DGC Jones. An analysis of the granularity of scattered optical maser light. *Physics Letters*, 7(5):321–323, 1963.
21. BM Oliver. Sparkling spots and random diffraction. *Proceedings of the IEEE*, 51(1):220–221, 1963.

22. HM Pedersen. Theory of speckle dependence on surface roughness. *JOSA*, 66(11):1204–1210, 1976.
23. JW Goodman. *Speckle phenomena in optics: theory and applications*, volume 1. Roberts and Company, 2007.
24. D Monaghan, D Kelly, B Hennelly, and B Javidi. Speckle reduction techniques in digital holography. In *Journal of Physics: Conference Series*, volume 206, page 012026. IOP Publishing, 2010.
25. CY Chen, WC Su, CH Lin, MD Ke, QL Deng, and KY Chiu. Reduction of speckles and distortion in projection system by using a rotating diffuser. *Optical review*, 19(6):440–443, 2012.
26. KV Chellappan, E Erden, and H Urey. Laser-based displays: a review. *Appl. Opt.*, 49(25):F79–F98, Sep 2010.
27. Y Aizu and T Asakura. Bio-speckle phenomena and their application to the evaluation of blood flow. *Optics & Laser Technology*, 23(4):205–219, 1991. ISSN 0030-3992.
28. Boas, D.A.; Yodh, A.G. Spatially varying dynamical properties of turbid media probed with diffusing temporal light correlation. *J. Opt. Soc. Am. A* 1997, 14, 192, doi:10.1364/josaa.14.000192.
29. Boas, D.A.; Campbell, L.E.; Yodh, A.G. Scattering and imaging with diffusing temporal field correlations. *Phys. Rev. Lett.* 1995, 75, 1855–1858, doi:10.1103/PhysRevLett.75.1855.
30. Mesquita, R.C.; Durduran, T.; Yu, G.; Buckley, E.M.; Kim, M.N.; Zhou, C.; Choe,

- R.; Sunar, U.; Yodh, A.G. Direct measurement of tissue blood flow and metabolism with diffuse optics. *Philos. Trans. R. Soc. A Math. Phys. Eng. Sci.* 2011, 369, 4390–4406, doi:10.1098/rsta.2011.0232.
31. Maret, G.; Wolf, P.E. Multiple light scattering from disordered media. The effect of brownian motion of scatterers. *Zeitschrift für Phys. B Condens. Matter* 1987, 65, 409–413, doi:10.1007/BF01303762.
32. Pine, D.J.; Weitz, D.A.; Chaikin, P.M.; Herbolzheimer, E. Diffusing wave spectroscopy. *Phys. Rev. Lett.* 1988, 60, 1134–1137, doi:10.1103/PhysRevLett.60.1134.
33. Pine, D.J.; Weitz, D.A.; Zhu, J.X.; Herbolzheimer, E. Diffusing-wave spectroscopy: dynamic light scattering in the multiple scattering limit. *J. Phys.* 1990, 51, 2101–2127, doi:10.1051/jphys:0199000510180210100.
34. Boas, D.A.; Pitris, C.; Ramanujam, N. *Handbook of biomedical optics*; 2016; ISBN 9781420090376.
35. Buckley, E.M.; Parthasarathy, A.B.; Grant, P.E.; Yodh, A.G.; Franceschini, M.A. Diffuse correlation spectroscopy for measurement of cerebral blood flow: future prospects. *Neurophotonics* 2014, 1, 011009, doi:10.1117/1.nph.1.1.011009.
36. Boas, D.A.; Campbell, L.E.; Yodh, A.G. Scattering and imaging with diffusing temporal field correlations. *Phys. Rev. Lett.* 1995, 75, 1855–1858, doi:10.1103/PhysRevLett.75.1855.
37. Cheung, C.; Culver, J.P.; Takahashi, K.; Greenberg, J.H.; Yodh, A.G. In vivo cerebrovascular measurement combining diffuse near-infrared absorption and correlation spectroscopies. *Phys. Med. Biol.* 2001, 46, 2053–2065,

doi:10.1088/0031-9155/46/8/302.

38. Li, J.; Dietsche, G.; Iftime, D.; Skipetrov, S.E.; Maret, G.; Elbert, T.; Rockstroh, B.; Gisler, T. Noninvasive detection of functional brain activity with near-infrared diffusing-wave spectroscopy. *J. Biomed. Opt.* 2005, 10, 044002, doi:10.1117/1.2007987.
39. “MD STARnet Data and Statistics.” *Centers for Disease Control and Prevention*, Centers for Disease Control and Prevention, 21 Nov. 2022, <https://www.cdc.gov/ncbddd/musculardystrophy/data.html>.
40. “Duchenne Muscular Dystrophy.” *Wikipedia*, Wikimedia Foundation, 9 Mar. 2023, https://en.wikipedia.org/wiki/Duchenne_muscular_dystrophy.
41. MR,; Paulson OB;Engel AG;Gomez. “Muscle Blood Flow in Duchenne Type Muscular Dystrophy, Limb-Girdle Dystrophy, Polymyositis, and in Normal Controls.” *Journal of Neurology, Neurosurgery, and Psychiatry*, U.S. National Library of Medicine, <https://pubmed.ncbi.nlm.nih.gov/4210685/>.
42. Author links open overlay panelAlexander R. Dietz a b, et al. “Intramuscular Blood Flow in Duchenne and Becker Muscular Dystrophy: Quantitative Power Doppler Sonography Relates to Disease Severity.” *Clinical Neurophysiology*, Elsevier, 4 Nov. 2019, <https://www.sciencedirect.com/science/article/abs/pii/S1388245719312593>.
43. Mendell JR;Shilling C;Leslie ND;Flanigan KM;al-Dahhak R;Gastier-Foster J;Kneile K;Dunn DM;Duval B;Aoyagi A;Hamil C;Mahmoud M;Roush K;Bird L;Rankin C;Lilly H;Street N;Chandrasekar R;Weiss RB; “Evidence-Based Path to Newborn Screening for Duchenne Muscular Dystrophy.” *Annals of Neurology*, U.S. National Library of Medicine, <https://pubmed.ncbi.nlm.nih.gov/22451200/>.

44. Bonilla E;Samitt CE;Miranda AF;Hays AP;Salviati G;DiMauro S;Kunkel LM;Hoffman EP;Rowland LP; “Duchenne Muscular Dystrophy: Deficiency of Dystrophin at the Muscle Cell Surface.” *Cell*, U.S. National Library of Medicine, <https://pubmed.ncbi.nlm.nih.gov/3042151/>.
45. Hoffman EP;Fischbeck KH;Brown RH;Johnson M;Medori R;Loike JD;Harris JB;Waterston R;Brooke M;Specht L; “Characterization of Dystrophin in Muscle-Biopsy Specimens from Patients with Duchenne's or Becker's Muscular Dystrophy.” *The New England Journal of Medicine*, U.S. National Library of Medicine, <https://pubmed.ncbi.nlm.nih.gov/3285207/>.
46. Kodippili K;Hakim CH;Yang HT;Pan X;Yang NN;Laughlin MH;Terjung RL;Duan D; “Nitric Oxide-Dependent Attenuation of Noradrenaline-Induced Vasoconstriction Is Impaired in the Canine Model of Duchenne Muscular Dystrophy.” *The Journal of Physiology*, U.S. National Library of Medicine, <https://pubmed.ncbi.nlm.nih.gov/30152022/>.
47. Kalchenko, Vyacheslav, et al. “A Robust Method for Adjustment of Laser Speckle Contrast Imaging during Transcranial Mouse Brain Visualization.” *MDPI*, Multidisciplinary Digital Publishing Institute, 13 July 2019, <https://www.mdpi.com/2304-6732/6/3/80>.
48. Abu Jawdeh, Elie G, et al. “Noncontact Optical Imaging of Brain Hemodynamics in Preterm Infants: A Preliminary Study.” *Physics in Medicine & Biology*, vol. 65, no. 24, 2020, p. 245009., <https://doi.org/10.1088/1361-6560/abc5a7>.
49. Boas, David A., and Andrew K. Dunn. “Laser Speckle Contrast Imaging in Biomedical Optics.” *Journal of Biomedical Optics*, vol. 15, no. 1, 2010, p. 011109., <https://doi.org/10.1117/1.3285504>.
50. Dragojević, Tanja, et al. “High-Density Speckle Contrast Optical Tomography of Cerebral Blood Flow Response to Functional Stimuli in The Rodent Brain.”

Neurophotonics, vol. 6, no. 04, 2019, p. 1.,
<https://doi.org/10.1117/1.nph.6.4.045001>.

51. *Dynamic Imaging of Cerebral Blood Flow Using Laser Speckle*.
<https://journals.sagepub.com/doi/10.1097/00004647-200103000-00002>.
52. K.; Bi R; Dong J; Lee. “Deep Tissue Flowmetry Based on Diffuse Speckle Contrast Analysis.” *Optics Letters*, U.S. National Library of Medicine,
<https://pubmed.ncbi.nlm.nih.gov/23632498/>.
53. Lee, Kijoon. “Diffuse Speckle Contrast Analysis (DSCA) for Deep Tissue Blood Flow Monitoring.” *Advanced Biomedical Engineering*, vol. 9, 2020, pp. 21–30.,
<https://doi.org/10.14326/abe.9.21>.
54. Lin, Chenhao P., et al. “Exploring the Feasibility of Fiber-Based Speckle Contrast Optical Spectroscopy.” *Optica Publishing Group*, Optica Publishing Group, 20 Apr. 2020, <https://opg.optica.org/abstract.cfm?uri=OCT-2020-JW3A.37>.
55. Liu C; Kılıç K; Erdener SE; Boas DA; Postnov DD; “Choosing a Model for Laser Speckle Contrast Imaging.” *Biomedical Optics Express*, U.S. National Library of Medicine, <https://pubmed.ncbi.nlm.nih.gov/34221679/>.
56. “Noninvasive Imaging of Cerebral Activation with Diffuse Optical Tomography.” *In Vivo Optical Imaging of Brain Function*, 2002, pp. 209–238.,
<https://doi.org/10.1201/9781420038491-13>.
57. Senarathna, Janaka, et al. “Laser Speckle Contrast Imaging: Theory, Instrumentation and Applications.” *IEEE Reviews in Biomedical Engineering*, vol. 6, 2013, pp. 99–110., <https://doi.org/10.1109/rbme.2013.2243140>.
58. Sie, Edbert J., et al. “High-Sensitivity Multispeckle Diffuse Correlation

Spectroscopy.” *Neurophotonics*, vol. 7, no. 03, 2020, <https://doi.org/10.1117/1.nph.7.3.035010>.

59. Sunwoo, John, et al. “Diffuse Correlation Spectroscopy Blood Flow Monitoring for Intraventricular Hemorrhage Vulnerability in Extremely Low Gestational Age Newborns.” *Scientific Reports*, vol. 12, no. 1, 2022, <https://doi.org/10.1038/s41598-022-16499-3>.
60. Valdes, Claudia P., et al. “Speckle Contrast Optical Spectroscopy, a Non-Invasive, Diffuse Optical Method for Measuring Microvascular Blood Flow in Tissue.” *Biomedical Optics Express*, vol. 5, no. 8, 2014, p. 2769., <https://doi.org/10.1364/boe.5.002769>.
61. Zhao, Mingjun, et al. “Extraction of Tissue Optical Property and Blood Flow from Speckle Contrast Diffuse Correlation Tomography (SCDCT) Measurements.” *Biomedical Optics Express*, vol. 12, no. 9, 2021, p. 5894., <https://doi.org/10.1364/boe.429890>.
62. Dietz, Alexander R., et al. “Intramuscular Blood Flow in Duchenne and Becker Muscular Dystrophy: Quantitative Power Doppler Sonography Relates to Disease Severity.” *Clinical Neurophysiology*, vol. 131, no. 1, 2020, pp. 1–5., <https://doi.org/10.1016/j.clinph.2019.09.023>.
63. “MCL-1500-1.75.” *MCL-1500-1.75 Coherent Image Bundle, Polyethylene Jacket*, <https://i-fiberoptics.com/fiber-detail-asahi.php?id=3305&sum=162>.
64. “Ninjaflex 3D Printer Filament (85a).” *NinjaTek*, 12 Apr. 2021, <https://ninjatek.com/shop/ninjaflex/>.
65. *Stabilized Compact Red Crystalaser*. <https://crystalaser.com/DL635-785.pdf>.

66. “Thorlabs - BS041 10:90 (R:t) Non-Polarizing Beamsplitter Cube, 700 - 1100 Nm, 1/2.” *Thorlabs, Inc. - Your Source for Fiber Optics, Laser Diodes, Optical Instrumentation and Polarization Measurement & Control*, <https://www.thorlabs.com/thorproduct.cfm?partnumber=BS041>.
67. “Thorlabs - LA1461-M1 ø1.” *Thorlabs, Inc. - Your Source for Fiber Optics, Laser Diodes, Optical Instrumentation and Polarization Measurement & Control*, <https://www.thorlabs.com/thorproduct.cfm?partnumber=LA1461-ML>.
68. “Thorlabs - MVL6X12Z 6.5x Zoom Lens with 12 Mm Fine Focus.” *Thorlabs, Inc. - Your Source for Fiber Optics, Laser Diodes, Optical Instrumentation and Polarization Measurement & Control*, <https://www.thorlabs.com/thorproduct.cfm?partnumber=MVL6X12Z>.
69. “Thorlabs - NE10A-B ø25 Mm Absorptive Neutral Density Filter, ARC: 650-1050 Nm, SM1-Threaded Mount, OD:1.0.” *Thorlabs, Inc. - Your Source for Fiber Optics, Laser Diodes, Optical Instrumentation and Polarization Measurement & Control*, <https://www.thorlabs.com/thorproduct.cfm?partnumber=NE10A-B>.
70. “Zyla 5.5 Scmos - Andor.” *Oxford Instruments*, <https://andor.oxinst.com/products/scmos-camera-series/zyla-5-5-scmos>.
71. “Evaluation of the Disability Determination Process for Traumatic Brain Injury in Veterans.” 2019, <https://doi.org/10.17226/25317>.